

# New regional insights into the stable water isotope signal at the northern Antarctic Peninsula as tools for climate studies

Francisco Fernandoy<sup>1</sup>, Dieter Tetzner<sup>2</sup>, Hanno Meyer<sup>3</sup>, Guisella Gacitúa<sup>4</sup>, Kirstin Hoffmann<sup>3</sup>, Ulrike Falk<sup>5</sup>

5 <sup>1</sup>Facultad de Ingenieria, Universidad Andres Bello, Viña del Mar, 2531015, Chile

<sup>2</sup>Center for Climate and Resilience Research, Universidad de Chile, Santiago, 8370361, Chile

<sup>3</sup>Alfred Wegener Institute Helmholtz Centre for Polar and Marine Research, Research Unit Potsdam, Telegrafenberg A43, 14473 Potsdam, Germany.

<sup>4</sup>Programa GAIA-Antártica, Universidad de Magallanes, Punta Arenas, 6210427, Chile

10 <sup>5</sup>Climate Lab, Geography Department, University Bremen, 28334 Bremen, Germany

*Correspondence to:* Francisco Fernandoy (francisco.fernandoy@unab.cl)

**Abstract.** The Antarctic Peninsula is one of the most challenging regions of Antarctica from a climatological perspective, owing to the recent atmospheric and oceanic warming. The steep topography and a lack of long-term and in situ meteorological observations complicate extrapolation of existing climate models to the sub-regional scale. Here, we present new evidence from the northern Antarctic Peninsula to demonstrate how stable water isotopes of firn cores and recent precipitation samples can reveal climatic processes related to nearby oceanic and atmospheric conditions. A noticeable effect of the sea ice cover on local temperatures and atmospheric modes, in particular the Southern Annular Mode (SAM), is demonstrated. In years with large sea ice extension in winter (negative SAM anomaly), an inversion layer in the lower troposphere develops at the coastal zone. Therefore, an isotope-temperature relationship valid for all seasons cannot be concluded. The  $\delta$ -T. relationship rather depends on seasonal variability of oceanic conditions. Transitional seasons (autumn and spring) are both stable seasons with an isotope-temperature gradient of  $+0.69\text{‰ }^{\circ}\text{C}^{-1}$ . The firn stable isotope composition reveals that the near-surface temperature at the most northern portion of the Antarctic Peninsula shows a decreasing trend ( $-0.33^{\circ}\text{C y}^{-1}$ ) between 2008 and 2014. Moreover, the deuterium excess ( $d_{\text{excess}}$ ) has been demonstrated to be a reliable indicator of seasonal oceanic conditions, and therefore suitable to improve a firn age model based on seasonal  $d_{\text{excess}}$  variability. The annual accumulation rate in this region is highly variable, ranging between  $1060 \text{ kg m}^{-2} \text{ y}^{-1}$  and  $2470 \text{ kg m}^{-2} \text{ y}^{-1}$  from 2008 to 2014. The combination of isotopic and meteorological data is a key for reconstructing climatic conditions with a high temporal resolution in polar regions where no direct observations exist.

## 1 Introduction

West Antarctica and especially the Antarctic Peninsula (AP) have been in the scope of the scientific community due to the notable effects of the present warming on the atmosphere, cryosphere, biosphere and ocean. The increase of air temperatures along the West Antarctic Peninsula coast (Carrasco, 2013) displays signs of a shifting climate system since the early 20<sup>th</sup> century (Thomas et al., 2009). Recently, rapid warming of both atmosphere and ocean is causing instability of ice shelves in West Antarctica, especially in some regions of the AP (Pritchard et al., 2012). The collapse of ice shelves triggers an accelerated ice-mass flow and discharge into the ocean, as the ice shelves' buttressing function gets lost. Several grounded tributary glaciers on AP and in West Antarctica recently loose mass to the oceans, and often at accelerated rates due to this phenomenon (Pritchard and Vaughan, 2007; Rignot et al., 2005; Pritchard et al., 2012), which in combination with surface snow melt, has contributed to a negative surface mass balance especially in the northern part of the AP region (Harig and Simons, 2015; Seehaus et al., 2015; Dutrieux et al., 2014; Shepherd et al., 2012).

The glaciers of the AP have lost ice mass at a rate of around  $27 (\pm 2) \text{ Gt y}^{-1}$  between 2002 and 2014, which combined with the mass loss over West Antarctic ice sheet of  $121 (\pm 8) \text{ Gt y}^{-1}$ , surpassed the positive mass balance observed in East Antarctica (Harig and Simons, 2015). This demonstrates how vulnerable the coastal region of West Antarctica is to increased air and sea surface temperatures (Bromwich et al., 2013; Meredith and King, 2005).

Surface snow and ice melt on the AP represents up to 20% of the total surface melt area (extent) and 66% of the melt volume of whole Antarctica for at least the last three decades (Trusel et al., 2012; Kuipers Munneke et al., 2012). Regional positive temperatures detected by remote-sensing techniques and ice-core data reveal that melt events have been temporally more wide-spread since the mid-20<sup>th</sup> century (Abram et al., 2013; Trusel et al., 2015), with some severe melt events during the first decade of the 21<sup>st</sup> century (Trusel et al., 2012). Increased surface melt and glacier calving may have an impact on the fresh water budget of the upper ocean layers and therefore on the biological activity of the coastal zone (Meredith et al., 2016; Dierssen et al., 2002). The most significant warming trend detected at the coast of the AP occurs during winter season, especially on the west side of the Peninsula, where a tendency  $>0.5^\circ\text{C decade}^{-1}$  for the period 1960–2000 has been reported at several stations (Turner et al., 2005; Carrasco, 2013). Winter warming is especially evident in the daily minimum and monthly mean temperature increase, as described by Falk and Sala (2015) for the meteorological record of the Bellingshausen Station at King George Island (KGI) at the northern AP during the last 40 years. In KGI the daily mean temperature during winter increased at about  $0.4^\circ\text{C decade}^{-1}$ , with a marked warming during August (austral winter) at a rate of  $+1.37 (\pm 0.3)^\circ\text{C decade}^{-1}$ . Positive temperatures even in winter are more commonly observed, leading to more frequent and extensive surface melting year-round especially for the northern AP, which is dominated by maritime climate conditions (Falk and Sala, 2015).

The mechanisms behind increasing atmosphere and ocean temperatures are still not completely understood but can be confidently linked to perturbations of regular (pre-industrial period) atmospheric circulation patterns (Pritchard et al., 2012; Dutrieux et al., 2014). Most heat advection to the southern ocean and atmosphere has been related to the poleward movement of the Southern Annular Mode (SAM) and to some extent to the El Niño Southern Oscillation (ENSO) (Gille, 2008; Dutrieux

et al., 2014; Fyfe et al., 2007). During the last decades, SAM has been shifting into a positive phase, implying lower than normal (atmospheric) pressures at coastal Antarctic regions (latitude 65°S) and higher (atmospheric) pressures over mid-latitudes (latitude 40°S) (Marshall, 2003). With lower pressures around Antarctica, the circumpolar westerly winds increase in intensity (Marshall et al., 2006). As a consequence, air masses transported by intensified westerlies overcome the topography of the AP more frequently, especially in summer, bringing warmer air to the east side of the AP (van Lipzig et al., 2008; Orr et al., 2008). The correlation between the SAM and the surface air temperatures is generally positive for the AP, explaining a large part (~50%) of near-surface temperature increase for the last half century (Marshall et al., 2006; Marshall, 2007; Carrasco, 2013; Thompson and Solomon, 2002). An enhanced circulation allows more humidity to be transported to and trapped at the west coast of the AP due to the orographic barrier of the central mountain chain. Therefore, the accumulation has consistently increased across the entire Peninsula during the whole 20<sup>th</sup> century, doubling the accumulation rate from the 19<sup>th</sup> century in the southern AP region (Thomas et al., 2008; Goodwin et al., 2015; Dalla Rosa, 2013).

The increase of greenhouse gas concentrations and the stratospheric depletion of the ozone layer, both linked to anthropogenic activity, are suggested to be the main forcing factors of the climate shift that affects the ocean-atmosphere-cryosphere system for at least the last half century (Fyfe and Saenko, 2005; Sigmond et al., 2011; Fyfe et al., 2007).

The lack of long-term meteorological records hampers accurately determining the onset and regional extent of this climate shift. Therefore, climate models are necessary to extend the scarce climate data both spatially and temporally. One major challenge is to correctly integrate the steep and rough topography of the AP into climate models. To realize this goal, direct information on surface temperatures, melting events, accumulation rates, humidity sources and transport pathways are urgently needed. As direct measurements of these parameters are not available, the reconstruction of the environmental variability, basically relies on proxy data such as the stable water isotope composition of precipitation, firn and ice (e.g.: Thomas and Bracegirdle, 2009; Thomas et al., 2009; Abram et al., 2013).

In this investigation, we focus on a stable water isotope-based, high temporal resolution assessment (seasonal resolution between austral autumn 2008 and austral summer 2015) of climate variables including accumulation rates, temperatures and melt events on the AP and their relationship to atmospheric modes and moisture-source conditions i.e. sea surface temperature, humidity and sea ice extent. We investigate the effects of the orographic barrier of the AP on the air mass and moisture transport, with increasing precipitation rates from the coast to the mountain range on the Peninsula divide at ca. 1100 m a.s.l. (Fernando et al., 2012), where the ice thickness reaches ca. 350 m at maximum (Cárdenas et al., 2014).

## **2 Glaciological setting and previous work**

Since 2008, we have undertaken several field campaigns to the northernmost region of the AP, where we have retrieved a number of firn cores of up to 20 m depth. The present investigation is the first of its kind for this sector of the AP. Other studies have been carried out further south at Detroit Plateau (Dalla Rosa, 2013) and Bruce Plateau (Goodwin et al., 2015), at around 100 and 400 km South-West of the northern AP. Nonetheless, not much is known about the glaciological conditions at the

northern tip of the AP and very few ice cores have been retrieved from this area despite of the high number of scientific stations in the region. The AP and Sub-Antarctic islands are principally characterized by mountain glaciers or small ice caps, which flow into the Bellingshausen and Weddell Sea to the West and East, respectively (Turner et al., 2009). Rückamp et al. (2010), noted that the ice cap covering the King George Island, South Shetlands (62.6°S, 60.9°W) is characterized by polythermal conditions and temperate ice at the surface ( $>-0.5^{\circ}\text{C}$ ), and is therefore sensitive to small changes in climatic conditions. Further South, Zagorodnov et al. (2012) showed that temperatures from boreholes reach a minimum at 173 m depth ( $-15.8^{\circ}\text{C}$ ) at Bruce Plateau (66.1°S, 64.1°W, 1975.5 m a.s.l.). Similar glaciological conditions were reported on the east side of the AP at James Ross Island (64.2°S, 57.8°W, 1640 m a.s.l.); (Aristarain et al., 2004). Accumulation rates at the northern AP are directly related to the westerly atmospheric circulation and maritime conditions, with values close to  $2000\text{ kg m}^{-2}\text{ y}^{-1}$  on the west side (Goodwin et al., 2015; Potocki et al., 2016) and lower values ( $\sim 400\text{ kg m}^{-2}\text{ y}^{-1}$ ) on the east side (Aristarain et al., 2004); ice thickness from all coring-sites reported is  $<500\text{ m}$  to the bedrock.

### 3 Methodology

#### 3.1 Field work and sample processing

During five austral summer campaigns (2008–2010, 2014, 2015), an altitudinal profile was completed from sea level near O'Higgins Station (OH) to 1130 m a.s.l at the Laclavere Plateau (LCL) (Fig. 1). In total, five firn cores were included in this paper: OH-4, OH-5, OH-6, OH-9, OH-10 (Fig. 1); coordinates and further details of the firn cores are given in Table 1. 210 daily precipitation samples were gathered at the meteorological observatory of the O'Higgins Station (57.90°W, 63.32°S, 13 m a.s.l.) during 2008–2009 (Fernandoy et al., 2012) and 2014 (Table 2). From these samples, around 6% (13 samples) were discarded from the analysis due to improper storing. This was indicated by unusual values of stable water isotope analyses, and were discriminated using a statistical outlier test (modified Thompson tau technique). Cores OH-4, OH-5, OH-6 and OH-9 were retrieved between 2008 and 2010 and analyzed for their stable water isotope composition and physical properties of ice as described in Fernandoy et al. (2012) and Meyer et al. (2000). Additionally, a density profile of OH-9 was obtained by using an X-ray microfocus computer tomograph at the ice-core processing facilities of the Alfred Wegener Institute, Helmholtz Centre for Polar and Marine Research in Bremerhaven, Germany (Linow et al., 2012). The X-ray tomography provides a very high-resolution (1mm) density profile of the physical properties of the ice. The core OH-10 was retrieved in 2015 using an electric drilling device with 5.7 cm inner diameter (Icedrill.ch AG). The retrieved core was first stored under controlled temperature conditions ( $-20^{\circ}\text{C}$ ) at the Chilean scientific station Prof. Julio Escudero (King George Island) and later transported to a commercial cold storage in Viña del Mar, Chile. The core sections were measured and weighted for density-profile construction and then sub-sampled with a 5 cm resolution for stable water isotope analysis. A visual logging and description of the cores were carried out to identify possible melt layers and their thicknesses. Subsequently, the samples were melted overnight at  $4^{\circ}\text{C}$  in a refrigerator at the Stable Isotope Laboratory of the Universidad Nacional Andrés Bello (UNAB), Viña del Mar, Chile. To avoid any evaporation, the 5cm samples were placed in sealed bags (Whirl-pak) and agitated for

homogenization before isotopic analysis. Firn and recent precipitation samples collected from OH in 2014 (Table 1) were analyzed by a liquid water stable isotope analyzer from Los Gatos Research (TLWIA 45EP), located at the UNAB facilities. Accuracy of the measurements is better than 0.1 ‰ for oxygen and 0.8 ‰ for hydrogen isotopes for all samples analyzed. All oxygen and hydrogen stable water isotope data of precipitation and firn core samples are presented in relation to the Vienna Standard Mean Ocean Water Standard (VSMOW) in ‰, as  $\delta^{18}\text{O}$  and  $\delta\text{D}$  for oxygen and hydrogen isotopes, respectively.

### 3.2 Database and time series analysis

Stable water isotope data were compared to major meteorological parameters from the region (Fig. 2). For this purpose, the following data sets were incorporated into our analysis: Near-surface air temperature ( $T_{\text{air}}$ ), precipitation amount (Pp) and sea-level pressure (SLP), recorded at the Russian Station Bellingshausen (BE) (58.96°W, 62.19°S, 15.8 m a.s.l.), available in daily and monthly resolution from the Global Summary of the Day (GSOD) data sets of the National Climatic Data Center (NCDC, available at: [www.ncdc.noaa.gov](http://www.ncdc.noaa.gov)) and the SCAR Reference Antarctic Data for Environmental Research (READER, available at: <https://legacy.bas.ac.uk/met/READER/>) (Turner et al., 2004). As temperature data from OH show several large record gaps, we considered the BE temperature corrected by a latitude difference (-1.4°C) for all further calculation at OH location, as for the estimation of air temperature on LCL. The BE data was considered for this calculation because of the high correlation with OH ( $R=0.97$ ,  $p<0.01$ ) and long-term consistency of the data (uninterrupted record since 1968). The correction is given by the linear regression between OH and BE temperature data. Other nearby stations like Esperanza (63.40°S, 57.00°W), were not considered because their slightly lower correlation ( $R=0.96$ ,  $p<0.01$ ) and likely higher continental influence on the temperature record. Sea surface temperature (SST) time series were extracted from the Hadley Centre observation datasets (HadSST3, available at: <http://www.metoffice.gov.uk/hadobs/hadsst3/>). The HadSST3 provides SST monthly means on a global 5° to 5° grid from 1850 to present (Kennedy et al., 2011a, b). Mean monthly SSTs were extracted from a quadrant limited by 60–65°S and 65–55°W. Missing data or outliers were interpolated from measurements taken in the neighbour quadrants. Relative humidity ( $rh$ ) time series were extracted from data obtained by the calculation of 3 day air parcel backward trajectories under isobaric conditions using the freely-accessible Hybrid single-particle Lagrangian integrated trajectory (HYSPLIT) model (<http://ready.arl.noaa.gov/HYSPLIT.php>). This three-dimensional model was fed with the global data assimilation system (GDAS) archives from NOAA/NCEP (Kanamitsu, 1989) to 1° latitude-longitude spatial coverage with a 1 hour temporal resolution and is available from 2006 to present (for more details visit: <http://ready.arl.noaa.gov/gdas1.php>). For studying the characteristics of air parcels approaching the AP,  $rh$  time series were obtained considering data from backward trajectories arriving at isobaric conditions (850 hPa) at OH station. SST and  $rh$  datasets were resampled to a regional scale defined by high-density trajectory paths (Bellingshausen and Weddell Seas). The resampled fields were defined by the spatial coverage of 1 day backward trajectories. The limits of the resulting quadrant extends from 98° W to 34° W longitude and from 47° S to 76° S latitude. The representativeness of this area is given because it geographically includes the region affected by westerly winds and sea ice front during winter time, both factors that exert high influence on the air parcels that

approach this region. A field horizontal mean of resampled  $rh$  values between sea level and 150 m a.s.l. was computed in this area to construct  $rh$  time series utilized throughout this work. Altitudinal temperature profiles were obtained from radiosonde measurements carried out at BE between 1979 and 1996 (SCAR Reference Antarctic Data for Environmental Research). Lapse rates were calculated from the temperature difference between sea level and the 850 hPa level. SAM index time series were obtained from the British Antarctic Survey (BAS, available at: <http://legacy.bas.ac.uk/met/gjma/sam.html>) (Marshall, 2003). Mean monthly sea ice extent around the AP (between 1979 and 2014) was obtained from the Sea Ice Index from the National Sea & Ice Data Center (NSIDC, available at <http://nsidc.org>). The measurements of sea-ice extension incorporated in this study considered as a starting point the coastal location of OH, and the sea-ice front in the direction towards KGI as an end point.

### 10 3.3 Stable Isotope time series analysis

The raw datasets obtained from stable water isotope analysis in firn cores produced low oscillation variance in the isotope-depth profiles. The measured isotope signals were considerably noisy, but values do not fluctuate far from the mean. There was a significant difference in the Standard Deviation (Sdev) values of oxygen isotopes between cores from lower altitudes (OH-4,  $\delta^{18}\text{O}$  Sdev = 1.2) versus cores from higher altitudes (OH-10,  $\delta^{18}\text{O}$  Sdev = 2.57) (Table 1). Furthermore, the patterns described in the isotope-depth profiles do not correspond to seasonal cycles. Despite several attempts to achieve a chronology by annual layer counting, the noise and the lack of consistent behavior in the isotope signals inhibited this interpretation. Difficulties from using conventional dating methodology for these firn cores led us to search for other ways to define the time scale of our signals. To realize this alternative methodology, the relationship between moisture source conditions and isotopic signature of precipitations was taken into account. Following the previous motivation, for each day when a precipitation sample was collected at OH, a 3 day air parcel backward trajectory was calculated using the HYSPLIT model with hourly resolution. Frequent air parcel paths were studied and monthly mean values of  $rh$  and SST from re-analysis data (GDAS) along these paths were calculated. Secondly, using the relationship between  $rh$  and SST calculated by Uemura et al. (2008), a theoretical value of deuterium excess ( $d_{excess\ meteo}$ ) was calculated for the OH station and nearby area (i.e.: northern Antarctic Peninsula) ( $d_{excess\ meteo} = -0.42 * rh + 0.45 * SST + 37.9$ ). Comparisons were made between the time series model for deuterium excess ( $d_{excess} = \delta\text{D} - 8 * \delta^{18}\text{O}$ ), derived from monthly mean values of the OH precipitation isotopic signal, and  $d_{excess\ meteo}$ , obtained from monthly mean values of  $rh$  and SST from the southern oceans.

At the same time, the  $d_{excess}$  signal obtained from stable isotope analysis of firn cores was represented into a signal with respect to the depth (i.e.: space domain). The  $d_{excess}$  isotope signal, was filtered using the Inverse Fast Fourier Transform (IFFT) in order to transform the space domain (depth) into a frequency representation of the isotope signal. To determine the best frequency of this mode, we analyzed the variation between the original signal and the signal obtained from each step of the Fast Fourier Transform (FFT) decomposition. By studying the progression of these variations, the frequency of the second mode showed the highest frequency, where the Sdev reaches an equilibrium. Thus, the final signal is only defined by a set of low frequencies.

Thereafter, the same procedure was applied to time series constructed with monthly means of  $d_{excess\ meteo}$  described previously. The strong similarities between the two signals, due to their dependency on the same variables (i.e.: environmental condition of the moisture source region), enabled the transformation from the depth domain of the  $d_{excess}$  signal (derived from measured stable isotope values) to time. This was made possible by using the common oscillation patterns in both profiles (by their IFFT), as time markers. After following this procedure,  $d_{excess}$  can be represented by an age model as shown in Fig. 3. Subsequently, monthly means of the firn cores isotope signal were calculated to generate time series for further analysis. Once the  $d_{excess}$  signals from firn cores were represented as time series, the same was done for  $\delta^{18}\text{O}$  records, by considering the time–depth constraints defined (Fig. 3).

## 4. Results

### 4.1 Precipitation samples

Table 2 and Fig. 4 show the stable isotope results, basic statistics and annual distribution of the precipitation samples collected at OH station, respectively. Combining  $\delta\text{D}$  and  $\delta^{18}\text{O}$  values from all precipitation samples allows for the definition of a Local Mean Water Line (LMWL):  $\delta\text{D} = 7.83 * \delta^{18}\text{O} - 0.12$ . Backward trajectory analysis of precipitation events reveals high–frequency transport across the Bellingshausen Sea in the last 24 hours before air parcels reach the AP (Fig. 5).

#### 4.1.1 Isotope–Temperature relationship

With the stable water isotope composition of single precipitation events and daily near–surface temperature ( $T_{\text{daily}}$ ), an isotope–temperature relationship was constructed for OH station using linear regression analysis. For this purpose, the sample set for each season was selected from the months with the largest number of samples (i.e. December 2008, March 2008 and–2009, June 2008 and October 2014). The purpose of this selection was to ensure larger datasets within a short period of time, with the aim of showing coherence and relation between  $\delta^{18}\text{O}$  and  $T$ . The linear regression between  $\delta^{18}\text{O}$  and  $T_{\text{daily}}$  based on 208 precipitation events revealed correlation coefficients ( $R$ ) higher than 0.6 and a statistical significance ( $p$ ) lower than 0.03 (t–statistic test significant at alpha 0.05). Outliers were discarded as explained in section 3.1 and later in 4.1.2. Furthermore, the same linear regression was performed for monthly averages calculated from daily events ( $T_{\text{monthly}}$ ;  $\delta^{18}\text{O}_{\text{monthly}}$ ) from the whole precipitation dataset ( $R= 0.3$ ,  $p>0.05$ ), over 24 months (February – 2008 to March – 2009, and April – November, 2014). Considerable differences were identified between the daily and monthly  $\delta^{18}\text{O}$ – $T$  relationships (Fig. 4a). The linear regression slope ( $s$ ) of austral autumn or MAM (March–April–May), considering the March 2008 and 2009 dataset to be representative of the MAM behavior, has shown to be quite near to  $s$  of austral spring or SON (September–October–November), considering the October 2014 dataset to be representative of the SON behavior:  $s= 0.77$  (standard error= 2.08,  $p<0.01$ ) and  $s= 0.61$  (standard error= 2.88,  $p=0.03$ ), respectively. If only the two datasets (MAM and SON) are taken into account together, a new linear regression can be defined as:  $\delta^{18}\text{O}= 0.79* T_{\text{daily}}-7.76$  ( $R= 0.74$ ,  $p<0.01$ , t–statistic test statistically significant at alpha 0.05). Thus, the time series of monthly averages shows a positive correlation between both parameters. An inverse behavior of  $s$  was

identified during July 2008 and June 2014, compared to MAM and SON. Following the same procedure, austral summer, or DJF (December-January-February), was represented by the sample set of December 2008 and austral winter or JJA (June-July-August) was represented by the sample set of June 2008, with  $s$  values of 1.17 ( $\delta^{18}\text{O} = 1.17 * T_{\text{daily}} - 8.19$ , standard error = 0.62,  $p = 0.01$ ) and 0.35 ( $\delta^{18}\text{O} = 0.35 * T_{\text{daily}} - 8.66$ , standard error = 1.74,  $p < 0.01$ ), respectively. Additionally, mean seasonal lapse rates obtained in this region show the highest values during DJF ( $-5.31 \text{ } ^\circ\text{C km}^{-1}$ ), similar values during MAM and SON ( $4.43 \text{ } ^\circ\text{C km}^{-1}$ , and  $-4.06 \text{ } ^\circ\text{C km}^{-1}$  respectively) and the lowest values during JJA ( $-2.73 \text{ } ^\circ\text{C km}^{-1}$ ) (Fig. 6).

#### 4.1.2 Deuterium excess – Temperature relationship

From stable water isotope information obtained from precipitation samples gathered at OH,  $d_{\text{excess}}$  values were calculated for each sample. Table 2 shows  $d_{\text{excess}}$  basic statistics for the dataset. Values of  $d_{\text{excess}}$  lower than  $-9 \text{ } \text{‰}$  (see Section 3.1) were filtered out in order to avoid disturbances in the model, as the quality of these samples may have been compromised during storage and transport. Daily  $d_{\text{excess}}$  values for the same months as specified in section 4.1.1 were compared with daily mean temperatures. Correlation coefficients for these comparisons are not significant ( $R > -0.42$  and  $R < 0.09$ ,  $p > 0.1$ , for negative and positive correlation period, respectively) and show variability. By comparing monthly temperature averages (calculated from daily events) to the datasets of 2008–2009 and 2014, the  $d_{\text{excess}}-T$  correlation coefficient improved (Fig. 4b). For the 2008–2009 dataset, we obtained a correlation coefficient of  $R = -0.77$  ( $p < 0.01$ ;  $T = -1 * d_{\text{excess}} + 1.53$ ; t-statistic test statistically significant at alpha 0.05). For the 2014 dataset, we obtained an  $R = 0.33$  ( $p > 0.05$ ;  $T = 0.17 * d_{\text{excess}} - 3.62$ ).

#### 4.1.3 Moisture source of precipitation

Three day air backward trajectories from precipitation events exhibit a wide distribution, originating spatially in both the Southern Pacific Ocean and the Amundsen–Bellingshausen Seas. The trajectories mainly derive from the Bellingshausen Sea, the Bransfield Strait and the Drake Passage, Tierra del Fuego and South America’s southern tip. Moreover, some trajectories ( $< 15\%$ ) originate from AP’s eastern side. Precipitation trajectories show an almost elliptically distributed pattern with a  $\text{N}40^\circ\text{W}$  orientation, where most follow pathways bounded by the latitudes  $60^\circ\text{S}$  and  $67^\circ\text{S}$ . The correlation between monthly mean values of  $d_{\text{excess}}$  (from precipitation samples) and  $d_{\text{excess meteorological}}$  (constructed from the meteorological parameters  $rh$  and SST of the high density precipitation pathways), showed a correlation coefficient of  $R = 0.86$  ( $p < 0.01$ ; t-statistic test statistically significant at alpha 0.05) (Fig. 7).

#### 4.2 Firn core samples from AP

Table 1 shows the stable isotope results and basic statistics for firn cores retrieved at the northern AP. The co-isotopic relationship  $\delta\text{D}-\delta^{18}\text{O}$  of each single firn core retrieved from LCL is analogous to the global meteoric water line (GMWL) and the local meteoric water line (LMWL) (Rozanski et al., 1993), with a mean slope of  $s = 7.91$  and an intercept of 3.64 (Fig. 8). These values are very close to those of the LMWL, although with a slightly higher intercept.



### 4.2.1 Age model based on stable water isotopes

Stable water isotope results from firn cores allow to derive depth profiles of  $\delta D$ ,  $\delta^{18}O$  and  $d_{excess}$  for each firn core. Lowest noise and the clearest seasonal patterns were found in  $d_{excess}$  profiles ( $d_{excess\ core}$ ) (Fig. 3), similar to findings published by Fernandoy et al. (2012). Due to the high correlation between  $d_{excess}$  from precipitation samples and  $d_{excess\ meteo}$  at sea level (see section 4.1.3), the correlation between  $d_{excess\ meteo}$  and  $d_{excess\ core}$  was evaluated. This was done to determine if the conditions of a coastal and oceanic–proximal moisture source were also represented and preserved in the  $d_{excess\ core}$  record to be used later as a chronology marker. The  $d_{excess\ core}$  signals were first filtered for their high frequency oscillation patterns and then the remnant signals compared with the high frequency filtered  $d_{excess\ meteo}$  monthly means (See section 3.3). The intercomparison between  $d_{excess\ meteo}$  and  $d_{excess\ core}$  illustrates a close similarity between them. Main peak–valley fitting between both signals leads to a monthly mean  $d_{excess\ core}$  signal represented on a defined time scale. The comparison between time series of monthly mean  $d_{excess\ core}$  and  $d_{excess\ meteo}$  data reveals correlation coefficients of  $R \geq 0.67$  ( $p < 0.01$ ; t-statistic test statistically significant at alpha 0.05) for all firn cores analyzed and obtained from 2006 to 2015. Table 3 summarizes correlation coefficients, statistical significances and time intervals for each firn core. From the firn cores retrieved from LCL, a single time series was constructed and then compared to the  $d_{excess\ meteo}$  time series in order to analyze the isotopic signal for the whole time interval. An even higher correlation coefficient of  $R = 0.75$  ( $p < 0.01$ ; t-statistics test statistically significant at alpha 0.05) was obtained between the two signals ( $d_{excess\ meteo}$  and  $d_{excess\ core}$ ). For the overlapping time interval in OH-9 and OH-10 (February 2012 to January 2014), we only considered data from OH-9, as these samples consist of more fresh and less compacted firn than the corresponding interval in OH-10. This in turn helps to avoid attenuation of the isotopic signal. Although we only considered OH-9 data for the overlapping time interval, we studied the changes in the standard deviation of the isotopic signal ( $\delta^{18}O$  and  $\delta D$ ) from both firn cores in the common time span. The standard deviation shows a decrease of 16% after one year of deposition in core OH-10 with respect to the same time interval in OH-9; and 2 to 3 years after the deposition the standard deviation of the signal decreases by 18%.

During visual firn core logging, thin and scarce melt layers were identified (mean width of  $\sim 1$  cm). The melt layers do not show evidence of infiltration nor have a clear pattern of distribution with depth (i.e. the association with summer layers). While analyzing the melt layers in relation to their time equivalent with depth, no clear pattern associated with a season was noted.

### 4.2.2 Seasonal temperature reconstruction from stable water isotopes

The age model developed using the  $d_{excess\ core}$  oscillation was later applied to construct a  $\delta^{18}O$  time series (Fig. 3). From this time series a periodical 2 year pattern was identified. This pattern is characterized by elevated values, higher than the  $\delta^{18}O$  monthly mean values between May and November in the years 2008, 2010, 2012 and 2014, which exhibit an inverse relationship to temperatures at BE. Between June and July in the following years 2009, 2011 and 2013,  $\delta^{18}O$  values are lower than the mean and exhibit a direct relationship to temperature at BE (Fig. 9). Therefore, the 2 year periodical pattern mentioned above is represented by even numbered years with austral winter  $\delta^{18}O$  values higher than the mean, followed by odd numbered

years with austral winter  $\delta^{18}\text{O}$  values lower than the mean. Monthly mean  $\delta^{18}\text{O}$  values were transformed to their temperature equivalent using the  $\delta^{18}\text{O}$ -T relationship obtained in section 4.1.1 from precipitation samples (Fig. 10), in order to investigate their seasonal behavior.

Calendar seasons in these latitudes does not follow regular patterns (i.e. DJF, MAM, JJA, SON), as seasonality largely depends on the sea ice cover during winter, often extending beyond calendar limits. Large sea ice extent (SIE) leads to a delayed onset of spring conditions. In this case winter-like conditions will be extended beyond August. Restricted sea ice extent on the contrary will lead to earlier spring-like conditions (before August). Depending on this conditions, we defined three seasons with their corresponding  $\delta^{18}\text{O}$ -T relationship. These seasons are: (1) an austral transitional season which considers the months from March to May and October–November (MAM-ON) (using precipitation datasets from March 2008–2009 and October 2014 for the  $\delta^{18}\text{O}$ -T relationship during that season,  $s=0.69$ ), (2) an austral winter season which considers the months from June to September (JJAS) (using precipitation datasets from June 2008 for the  $\delta^{18}\text{O}$ -T relationship during that season,  $s=0.35$ ), and (3) an austral summer season which considers months from December to February (DJF) (considers precipitation datasets from December 2008 for the  $\delta^{18}\text{O}$ -T relationship during that season,  $s=1.17$ ) (compare  $\delta^{18}\text{O}$ -T relationship functions in section 4.1.1). Despite this main seasonal classification for the use of the  $\delta^{18}\text{O}$ -T relationship, some particular seasons showed variable behavior when compared to the mean seasonal behavior in the time span covered in this study. In those cases, the seasonal behavior was extended or contracted beyond the boundaries of the main season classification depending on the SIE.

#### 4.2.3 Air temperature trends at Laclavere Plateau

Using the linear correlation between meteorological data: monthly lapse rates in BE, winter SAM index and SIE from OH (Fig. 11), a monthly temperature mean estimate that can be expressed by the equation  $T_{\text{LCL}} = (T_{\text{BE}} - 1.4) + 1.13 (M_{\text{month}} * \text{SIE}_{\text{OH}} + N_{\text{month}})$ , during the months when sea ice is developed (from May to September) and where  $M_{\text{month}}$  and  $N_{\text{month}}$  represent the slope and intercept of the monthly lapse rate–SIE relationship, respectively. During the months when there is no sea ice (from October to April) the monthly temperature can be expressed by the equation  $T_{\text{LCL}} = (T_{\text{BE}} - 1.4) + 1.13 * H(t)$ , where  $H(t)$  is the monthly mean lapse rate value of the month  $t$  measured in BE between 1978-1996. Considering this variables, a mean annual air temperature of  $-7.5^\circ\text{C}$  with a trend of  $-0.18^\circ\text{C year}^{-1}$  (statistically not significant at  $p=0.05$ ) was estimated on LCL for the time period 2009-2014. On the other hand, considering the  $\delta^{18}\text{O}$  time series data and the isotope–T relationship, a mean annual air temperature of  $-6.5^\circ\text{C}$  with a trend of  $-0.33^\circ\text{C year}^{-1}$  (statistically not significant at  $p=0.05$ ) was estimated on LCL for the years 2009-2014. The comparison between monthly mean temperature on LCL, estimated using the  $\delta^{18}\text{O}$  signal from firn cores and  $T_{\text{LCL}}$  estimated using the coupled effect of the latitude–corrected temperature record from BE,  $\text{SIE}_{\text{OH}}$  and lapse rates from BE, reveals a correlation coefficient of  $R= 0.7$  ( $p<0.01$ ; t-statistics test statistically significant at alpha 0.05). Both signals show a synchronous behavior, also with respect to the air temperature record at OH station. No statistically

significant direct correlation was observed between coastal stations (OH and BE) temperature records and the stable water isotope composition of firn cores.

#### 4.2.4 Accumulation rates

Density measurements from firn cores were used to construct density–depth profiles. Along these profiles a significant increase of density with depth was obtained. Linear regressions across different sections represent a normal firn compaction process reaching the snow–firn–density boundary ( $550 \text{ kg m}^{-3}$ ) at the 15.2 m depth. Using these linear regressions and considering the depth intervals delimited in section 4.2.1 as monthly values, we were able to estimate accumulation rates for different years. By using this procedure, we have estimated a mean accumulation rate of  $1770 \text{ kg m}^{-2} \text{ y}^{-1}$  at LCL between 2008 and 2015. The highest accumulation was found in 2008 ( $>2470 \text{ kg m}^{-2}$ ), then the rate noticeably decreased until 2015 ( $1600 \text{ kg m}^{-2}$ ) with its absolute minimum in 2010 ( $1060 \text{ kg m}^{-2}$ ) (Fig. 12a). A seasonal trend was observed, reflecting a decrease in the accumulation rates during JJA and SON between 2008 and 2015, which is responsible for the overall decreasing rates. On the other hand, the highest accumulation occurs during MAM and SON seasons (Table 4). Accumulation rate estimations derived from cores OH-9 and OH-10 for the common period in 2012 – 2013 differ only by about 3%. Other cores from the western flank of the Peninsula (OH-4, OH-5 and OH-6) show that the accumulation in 2008 (common period) depends on the altitude, with increasing values from the lower region to the highest point on LCL (Fig. 12b). The increase rate was about  $1500 \text{ kg m}^{-2} \text{ km}^{-1} \text{ y}^{-1}$  from 350 m a.s.l. to 1130 m a.s.l. in 2008.

## 5 Discussion

### 5.1 Stable water isotope fractionation processes and the local temperature relationship

The stable water isotope composition of precipitation samples from the 2008 and 2014 datasets show a high interannual similarity to each other, as well as to firn cores from the western flank and from LCL Plateau at AP (OH-4 to OH-10). Comparing the  $\delta^{18}\text{O}$  signal from OH-6 with data from precipitation samples at OH and with two other cores from the western side of the AP (OH-4 and OH-5) during a common period (March 2008 – August 2008), a  $\delta^{18}\text{O}$  decrease of  $-0.085\text{‰ km}^{-1}$  was found with increasing distance from the coast (Fig. 13a). The same data set was used to study the  $\delta^{18}\text{O}$ –altitude relationship. The  $\delta^{18}\text{O}$  seasonal means show an altitude dependency that yields seasonal  $\delta^{18}\text{O}$ –altitude patterns. During MAM a clear decrease of  $\delta^{18}\text{O}$  with height ( $-2.4\text{‰ km}^{-1}$  from sea level at OH up to LCL) is found, whereas during JJA no decreasing  $\delta^{18}\text{O}$  trend is obtained from sea level to 1130 m a.s.l. (Fig. 13b).

Moreover, further agreement can be found to several meteorological and climatic parameters as well as to reanalysis data. Backward trajectory analysis revealed that the most frequent pathways for air parcels that reach the northern part of AP derive from the Bellingshausen Sea, between  $55^{\circ}\text{S}$  and  $60^{\circ}\text{S}$  (Fig. 5) throughout the year. In contrast, localities further south on the AP and in West Antarctica, Ellsworth Land and coastal Ross Sea, respectively, exhibit a stronger continental influence on the precipitation source, depending on seasonal and synoptic scale conditions (Thomas and Bracegirdle, 2015; Sinclair et al.,

2012). The LMWL obtained from precipitation samples at OH ( $m=7.83$ ) is similar to the Antarctic meteoric water line obtained by Masson-Delmotte et al. (2008) ( $m=7.75$ ), and to the GMWL as presented by Rozanski et al. (1993) ( $m=8.13$ ). The similarity between the slope of LMWL and GMWL indicates that the fractionation processes during condensation mostly take place under thermodynamic equilibrium (Moser and Stichler, 1980). These results are consistent with those obtained by other authors for King George Island (Simões et al., 2004; Jiahong et al., 1998). Combining the stable water isotope signature of OH precipitation with time series of meteorological data representative for the conditions prevailing on the ocean near OH station, a strong relationship with  $rh$  and SST at the moisture source can be derived. This relationship has been well established, especially for the coastal Antarctic region where moisture transport from the source is generally short-ranging (Jouzel et al., 2013). The correlation between the  $d_{excess}$  of precipitation and a theoretical  $d_{excess\,meteo}$  derived from time series of meteorological data from the surrounding region has shown that both datasets are highly correlated ( $R=0.86$ ). Based on this evidence, we suggest that the Bellingshausen Sea constitutes the most important source of water vapor for precipitation for the study region at the northern AP. A similar conclusion was drawn for regions further south at the Peninsula (Thomas and Bracegirdle, 2015), however, with an increase of contributions from other local sources (e.g.: Amundsen Sea and continental conditions) to the local precipitation. This has also been observed at the northern AP, where some precipitation events that exhibited a stable water isotope composition beyond the normal range for the region (e.g. 20 August 2009,  $\delta^{18}O = -19.4\text{‰}$ ), were associated with uncommon sources of humidity as also recognized by the backward trajectory analysis.

The changing seasonal  $\delta^{18}O$ - $T$  relationship obtained from precipitation samples shows that the relationship between air temperature and condensation temperature varies throughout the year. The strong similarity in the  $\delta^{18}O$ - $T$  relationship during MAM and SON contrasts with the pronounced difference of this relationship between DJF and JJA. This highlights the variability of the  $\delta^{18}O$ - $T$  relationship along the whole year at the northern AP. Although the  $\delta^{18}O$ - $T$  correlations, presented in this study, were calculated from precipitation samples of particular months and years, which can certainly induce some bias. However, considering these datasets give a rough idea of the variations that can be seen in between seasons in this region. Furthermore, the  $\delta^{18}O$ - $T$  correlations obtained for MAM and SON ( $0.77\text{‰ }^{\circ}C^{-1}$  and  $0.61\text{‰ }^{\circ}C^{-1}$ , respectively) are similar to the values obtained by other authors for the AP (Aristarain et al., 1986; Peel et al., 1988). Even though the considered dataset is capable of representing variations within the time span covered by this study, it is too short to build a consistent baseline for the region. Despite the seasonal temperature difference is reduced in coastal sites, the difference in the seasonal  $\delta^{18}O$ - $T$  relationship suggests the existence of processes that disrupt the direct linkage between condensation temperature and surface air temperature. The inverse relationship between the  $\delta^{18}O$  signal from LCL ice cores and BE (and OH) monthly mean temperatures (Fig. 9 and 10), which is noticeable in some years during JJA, contrasts with the commonly accepted seasonal behavior characterized by a direct relationship between  $\delta^{18}O$  and surface air temperatures (Clark and Fritz, 1997). This particular behavior could be related to strong variations in meteorological conditions in the area between BE (OH) and LCL throughout the whole year. Therefore, air temperature on LCL was estimated by two independent methods: lapse rates (vertical temperature gradients) and  $\delta^{18}O$ - $T$  equivalents. The best correlation between both LCL temperatures estimations was obtained when an extended seasonal behavior was considered ( $R=0.7$ ;  $p<0.01$ ). This result is in agreement with the natural seasonal

variability in high latitudes, where the effects of some seasons extend beyond the calendar seasonal temporal limits related to the SIE, as previously explained. Without taking this seasonal variability into account would lead to a misinterpretation of the air temperature reconstruction for LCL, since the  $\delta^{18}\text{O}$ -T correlation would then be rather poor ( $R= 0.42$ ) and not reflecting the true seasonality in this region. The high similarity in the  $\delta^{18}\text{O}$ -T relationship during MAM and SON can be explained by the seasonal transition between summer and winter, when oceans surrounding the northern AP pass from ice-free to fully ice-covered conditions (or vice versa), respectively. Likely, ice-free ocean conditions are related to seasonal oscillations, which are highly dependent on atmospheric circulation patterns. In this sense, years with a marked negative SAM anomaly are associated with ice-covered sea conditions, whereas positive SAM phases are associated with ice-free sea conditions (Fig. 11). Other studies (Turner et al., 2016) point to a similar interaction between surface air temperature and SIE at AP and recognized that the SIE's inter-annual variability is related to atmospheric modes. This supports our own observations in a way that the sea ice is important for regulation of surface air temperatures in the region.

In firn cores obtained from the AP, average values from both  $\delta^{18}\text{O}$  and  $\delta\text{D}$  decrease as elevation increases to LCL (1130 m a.s.l.), which supports the altitudinal isotope effect identified by Fernandoy et al. (2012) for the region. In addition, standard deviations of seasonal (monthly mean)  $\delta\text{D}$  and  $\delta^{18}\text{O}$  values of firn cores from LCL are low and similar to those of firn cores from lower altitudes. Despite the variations in isotopic composition with height, in all firn cores the  $\delta\text{D}$ - $\delta^{18}\text{O}$  co-isotopic correlation is very similar to the LMWL obtained from precipitation samples at OH. This provides evidence of the uniformity of the fractionation conditions during the condensation process. Although a slight isotopic smoothing effect was distinguished between the cores (16% after one year of deposition), the distortions caused by post-depositional effects that may alter or homogenize the isotopic signal at this site, such as diffusion, can be considered as limited. The latter indication is well supported by the high accumulation rate in the region that does not allow a prolonged exposition of the freshly fallen snow to the atmosphere. Furthermore, the absence of significant infiltration and percolation associated with melting and refreezing events and the lack of a relationship between ice layers and seasons as well as with the stable water isotope record implies that the isotopic composition is not altered by surface melt infiltration and percolation. Thus, this reassures that post-depositional processes in the LCL region are negligible in the time period analyzed and that ice layers likely developed by wind ablation on wind-scouring processes at the plateau. Although these observations are in agreement with the results obtained in this region by Fernandoy et al. (2012) and Aristarain et al. (1990), several studies (Fernandoy et al., 2012; Simões et al., 2004; Travassos and Simoes, 2004; Jiahong et al., 1998) have identified a significant amount of melt layers in firn cores, mainly from KGI and from the western side of the AP at altitudes below 700 m a.s.l. The limited effect of post-depositional processes due to the high accumulation rates and to the ice layers reducing diffusion (Stichler et al., 2001), along with the high correlation between  $d_{\text{excess meteo}}$  and  $d_{\text{excess cores}}$ , confirm that the isotopic variations observed in firn core isotope records are mostly related to isotopic fractionation occurring during condensation and to  $rh$  and SST conditions in the vapor source regions.

## 5.2 Firn age model and accumulation rates

The stable water isotope signal obtained from firn cores shows no regularity in its seasonal behavior and lacks a clear annual oscillation pattern, likely because of the strong maritime influence (Clark and Fritz, 1997). These two criteria prevent the development of an age model by conventional annual layer counting in the isotope record (Legrand and Mayewski, 1997). In this context, the  $d_{excess}$  parameter represents a robust time indicator, as it has shown to be principally dependent on  $rh$  and SST conditions prevailing in the eastern Bellingshausen Sea where these variables are relatively stable (Jouzel et al., 2013). The high correlation coefficients (and high statistical significance) obtained for the relationship between  $d_{excess}$  and  $d_{excess\ meteo}$ , as shown in section 4.2.1, demonstrate that the method used to construct a time series is effective in dating isotope records of firn cores from the northern AP, even at a monthly resolution.

The most frequent  $d_{excess}$  values found in the firn cores (3‰ – 6‰) are in agreement with a strong coastal influence scenario as determined by Petit et al. (1991), implying that the  $d_{excess}$  relates to  $rh$  and SST of the humidity source and not to surface air temperature (Jouzel et al., 2013). Saigne and Legrand (1987), postulated that  $rh$  conditions prevailing at the sea surface have an important effect on the  $d_{excess}$  signal of precipitation below 2000 m a.s.l in the study region. The stable water isotope results, in combination with the meteorological records presented in this work, show that precipitation on LCL is highly correlated with  $rh$  and SST conditions in the Bellingshausen Sea near the AP.

The irrelevance of post-depositional effects along with the flat topography on LCL suggests that the estimate of accumulation rates from firn cores is representative of the amount of snow originally precipitated. Moreover, the slight smoothing of the isotope signal effect after deposition as well as the small differences in the accumulation rate observed for the common time period of firn cores OH-9 and OH-10, demonstrates that our age model is reliable, as two different data sets yield similar estimations for a common period. The results obtained allow to classify LCL as a high annual snow accumulation site (Table 4), closely following the estimations of other authors on King George Island dome (Bintanja, 1995; Zamoruyev, 1972; Jiahong et al., 1998) and on the AP further south of LCL (Dalla Rosa, 2013; Goodwin, 2013; van Wessem et al., 2015), of around 2000 – 2500 kg m<sup>-2</sup> y<sup>-1</sup>, but differs from the accumulation rate obtained by Simões et al. (2004) and Jiankang et al. (1994) on King George Island dome (600 kg m<sup>-2</sup> y<sup>-1</sup>). A seasonal bias of the accumulation was noted, with more favorable conditions for accumulation (i.e. higher precipitation amount) during autumn resulting from more synoptic scale features approaching the AP (Table 4).

## 5.3 Seasonal variability and disruption of atmospheric conditions

The depletion of  $\delta^{18}\text{O}$  with increasing height (altitude effect) and the simultaneous increase in accumulation along the western side of AP at LCL latitude can be explained with the help of an orographic precipitation model as proposed by Martin and Peel (1978). This model states that moist air parcels from the Southern Ocean are forced to ascend and cool down when approaching the AP due to the steep topography forming an orographic barrier to westerly winds. The depletion observed in  $\delta^{18}\text{O}$  reflects the strength of the fractionation process taking place within a short distance and in a low temperature environment (Fig. 14a).

Therefore, the isotopic fractionation process occurring at the AP and the direct linear relation between  $\delta^{18}\text{O}$  and condensation temperature allow us to study the temperature behavior with respect to the altitude increase on the basis of  $\delta^{18}\text{O}$  variations (Craig, 1961). However, whereas MAM air temperatures show a clear decrease with increasing height (atmospheric instability of the lower troposphere), JJA air temperatures exhibit an increase from sea level to 350 m a.s.l (atmospheric stability). At higher altitudes, a decreasing temperature trend is observed (atmospheric instability). The break at 350 m a.s.l during JJA could indicate the existence of a strong stratification within the lower troposphere on the western side of the AP. In addition, the variations in monthly mean lapse rates measured by radiosondes in BE throughout the year, provide evidence for the existence of a process that modifies the behavior of the lower troposphere, decreasing the lapse rate (between sea level and 850 hPa) during JJA and considerably increasing it during DJF (Fig. 15).

10 The close linear relationship identified between lapse rate magnitude and SIE indicates that SIE is an important factor for the development of these variations, especially between May and September.

The phenomenon previously described is likely linked to the development of an inversion layer in the lower troposphere on the western side of the AP mainly during JJA, which in turn is related to a strong radiative imbalance. During JJA, solar radiation diminishes until it reaches a minimum at the winter solstice. The lack of solar radiation leads to considerable cooling that favors the formation of sea ice and in turn, causes differential cooling between the sea ice surface and the air above it. As the sea ice surface cools faster than the air above it, a near-surface altitudinal pattern of increasing temperature develops where local atmospheric stability prevails. The layer of atmospheric stability extends from sea level up to at least 350 m a.s.l, where it turns into an atmospheric instability regime. Both regimes together favor the decrease of the overall lapse rate, as temperature first increases and then decreases with height. Conversely, no inversion layer is formed during DJF due to the absence of sea ice and hence, atmospheric instability prevails, which is related to high lapse rates (Fig. 14b and 14c).

25 The existence of an inversion layer during the months with sea ice coverage might explain the low oscillation of monthly mean temperatures estimated at LCL compared to monthly mean air temperatures at BE (OH). The inverse relation between SAM index and SIE also seems to play an important role, as SAM positive phases enhance the transport of warm and moist air towards the western side of the AP, thus inhibiting the formation of sea ice. This has a direct impact on the lapse rate as the development of an inversion layer is hindered and therefore air temperatures on LCL are regulated. The interaction between SAM and SIE plays a key role as sea-ice-covered conditions temper the maritime system, favoring continental-like conditions and reducing annual mean air temperature, implying a higher temperature amplitude in BE and OH throughout the year.

The temperature time series estimated from the stable water isotope record ( $\delta^{18}\text{O}$  and  $d_{\text{excess}}$ ) from LCL firn cores exhibits a periodic (biannual) pattern, which can be linked to a similar periodical behavior observed in SAM index and in SIE. The relatively constant temperatures observed during MAM, JJA and SON in years with a positive SAM phase provide evidence that during these seasons condensation is taking place at similar temperatures. Under such conditions (positive SAM), the low variations in the lapse rate throughout the year, along with the low thermal oscillation in BE (OH) explain the presence of a constant condensation temperature, which does not differ much from air temperature during DJF. Conversely, the stronger

annual temperature oscillation observed on LCL during negative SAM phases indicates marked variations in condensation temperature throughout the year.

Finally, the proposed inversion layer model (Fig. 15) explains the seasonal variations observed in the  $\delta^{18}\text{O}$ -T relationship of precipitation samples from OH. The distortion of the direct relation between condensation temperature and surface air temperature by an inversion layer makes it necessary to differentiate  $\delta^{18}\text{O}$ -T relationship according to the lapse rate evolution throughout the year. In this context, MAM and SON were identified as transitional periods in the formation of the inversion layer, mainly because of the sea-ice formation and retreat during these seasons. The seasonal adjustment considered to estimate LCL temperatures must be applied, because the sea-ice cover varies inter-annually in its duration and extension, which in turn produces the inter-annually variable inversion layer. The proposed model for the coastal region on the western side of the AP at OH latitude, is consistent with the observations of Yaorong et al. (2003) on KGI (South Shetland Islands), where several inversion layers developed extending beyond 400 m a.s.l.

## 6 Conclusions

In this study, we examined one of the most complete records of recent precipitation from the northern AP, with a total of 210 single precipitation events and more than 60 m of firn cores. The firn cores retrieved in this work include the accumulation at the northwestern AP region between 2008 and 2014. Precipitation and firn stable water isotope compositions have been compared to different meteorological data sets to determine their representativeness as climate proxies for the region.

The results of our study reveal significant seasonal changes in the  $\delta^{18}\text{O}$ -T relationship throughout the year. For autumn and spring a  $\delta^{18}\text{O}$ -T ratio of  $0.69\text{‰ } ^\circ\text{C}^{-1}$  ( $R=0.74$ ) was found to be most representative, whereas for winter and summer the  $\delta^{18}\text{O}$ -T ratio appears to be highly dependent on SIE conditions. The apparent moisture source for air parcels precipitating at the northern AP is mainly located in the Bellingshausen Sea and in the southern Pacific Ocean. The transport of water vapor along these oceanic and coastal pathways exerts a strong impact on the  $d_{\text{excess}}$  signal of precipitation. The comparison between the  $d_{\text{excess}}$  signal from the moisture source and the  $d_{\text{excess}}$  signal from firn cores has been used successfully to date the firn cores from the northern AP, yielding a seven-year isotopic time series in high temporal resolution for LCL.

Based on our dating method we could define LCL as a high snow accumulation site, with a mean annual accumulation rate of  $1770 \text{ kg m}^{-2} \text{ y}^{-1}$  for the period 2006–2014. Accumulation is highly variable from year to year, with a maximum and minimum of  $2470 \text{ kg m}^{-2}$  (in 2008) and  $1060 \text{ kg m}^{-2}$  (in 2010), respectively. In addition, we identified the presence of a strong orographic precipitation effect along the western side of the AP reflected by an accumulation increase with altitude ( $1500 \text{ kg m}^{-2} \text{ y}^{-1} \text{ km}^{-1}$ ), as well as by the isotopic depletion of precipitation from sea level up to LCL ( $-2.4\text{‰ km}^{-1}$  for autumn) and from the coast line up to the ice divide ( $-0.08 \text{‰ km}^{-1}$ ).

The maritime regime present on the western side of the AP has a strong control on air temperatures, observed as restricted summer/winter oscillation, and is reflected in a poor seasonality of the  $\delta^{18}\text{O}$  and  $\delta\text{D}$  profiles in firn cores. Recent climatic conditions can be only reconstructed from  $\delta^{18}\text{O}$  time series obtained from LCL firn cores when considering an inversion layer



model during winter season. The strength of the inversion layer likely depends on SIE and SAM index values. Taking into account the effect of the inversion layer on the isotope–temperature relationship, we observe a slight cooling trend of mean annual air temperature at LCL with an approximate rate of  $-0.33^{\circ}\text{C y}^{-1}$  for the period sampled by the examined firn cores (2009-2014). This finding is in line with evidence from stacked meteorological record of the nearby research stations as determined by Turner et al. (2016).

Our results demonstrate that the stable water isotope composition of firn cores retrieved from LCL is capable of reproducing the meteorological signal present in this region, validating it as a valuable proxy for paleo–climate reconstructions in the northern AP region. Environmental (atmosphere and ocean) and glaciological conditions present at LCL, a ~350 m thick ice cap, together with an almost undisturbed isotopic record are optimal prerequisites for the preservation of a climate proxy record with a high temporal resolution. Consequently, LCL is a suitable site for recovering a medium–depth ice core to investigate climate variations during the last centuries in the northern AP region.

## 6 Acknowledgements

The present work was funded by the FONDECYT project 11121551 and supported by the Chilean Antarctic Institute (INACH), the Chilean Air Force and Army logistic facilities. We want to show our gratitude to the Universidad Nacional Andres Bello for supporting this study. We also greatly thank our colleagues, who made field work conditions less severe, especially to Daniel Rutllant for his support on the logistic and field safety. We would like to thank all people involved on the laboratory work, especially to Ivonne Quintanilla, who carried out the sample processing at UNAB and to Dr. Johannes Freitag, for his support with the X-Ray tomography processing at AWI. Tracy Wormwood is greatly thanked for her support editing this manuscript. We highly appreciate the comments of two anonymous reviewers, who provided helpful observations that greatly contributed to improve this manuscript. Finally, we thank the dedicated work of the editor of this article Benjamin Smith.

## References

- Abram, N. J., Mulvaney, R., Wolff, E. W., Triest, J., Kipfstuhl, S., Trusel, L. D., Vimeux, F., Fleet, L., and Arrowsmith, C.: Acceleration of snow melt in an Antarctic Peninsula ice core during the twentieth century, *Nature Geosci*, 6, 404-411, doi: 10.1038/ngeo1787, 2013.
- Aristarain, A., Jouzel, J., and Pourchet, M.: Past Antarctic Peninsula climate (1850-1980) deduced from an ice core isotope record, *Climatic Change*, 9, 69-89, 1986.
- Aristarain, A., Jouzel, J., and Lorius, C.: A 400 Year Isotope record of the Antarctic Peninsula climate, *Geophys. Res. Lett.*, 17, 2369-2372, doi: 10.1029/GL017i013p02369, 1990.
- Aristarain, A., Delmas, R., and Stievenard, M.: Ice-Core Study of the link between Sea-Salt aerosol, Sea-Ice cover and climate in the Antarctic Peninsula Area, *Climatic Change*, 67, 63-86, 2004.
- Bintanja, R.: The local surface energy balance of the Ecology Glacier, King George Island, Antarctica: measurements and modelling, *Antarctic Science*, 7, 315-325, doi: 10.1017/S0954102095000435, 1995.
- Bromwich, D. H., Nicolas, J. P., Monaghan, A. J., Lazzara, M. A., Keller, L. M., Weidner, G. A., and Wilson, A. B.: Central West Antarctica among the most rapidly warming regions on Earth, *Nature Geosci*, 6, 139-145, doi: 10.1038/ngeo1671, 2013.

- Cárdenas, C., Johnson, E., Fernandoy, F., Meyer, H., Cereceda, F., and Vidal, V.: Preliminary results of the superficial and sub-glacier topography survey using Radio Echo Sounding at the La Claveré Plateau, Antarctic Peninsula, SCAR Open Science Conference, Auckland, New Zealand, 1-3 September, 2014.
- 5 Carrasco, J. F.: Decadal Changes in the Near-Surface Air Temperature in the Western Side of the Antarctic Peninsula, *Atmospheric and Climate Sciences*, 03, 7, doi: 10.4236/acs.2013.33029, 2013.
- Clark, I., and Fritz, P.: *Environmental Isotopes in Hydrogeology*, edited by: Stein, J., and Starkweather, A., Lewis, Boca Raton, New York, 311 pp., 1997.
- Craig, H.: Isotopic variations in meteoric waters, *Science*, 133, 1702-1703, doi: 10.1126/science.133.3465.1702, 1961.
- 10 Dalla Rosa, J.: Variabilidade da taxa de acumulação de neve no Platô Detroit, Península Antártica, M.S. thesis, Instituto de Geociências, Universidade Federal do Rio Grande do Sul, Porto Alegre, 98 pp., 2013.
- Dierssen, H. M., Smith, R. C., and Vernet, M.: Glacial meltwater dynamics in coastal waters west of the Antarctic peninsula, *Proceedings of the National Academy of Sciences*, 99, 1790-1795, doi: 10.1073/pnas.032206999, 2002.
- Draxler, R. R., and Hess, G. D.: An Overview of the HYSPLIT-4 modelling system for trajectories, dispersion and deposition, *Aust. Meteorol. Mag.*, 47, 295-308, 1998.
- 15 Dutrieux, P., De Rydt, J., Jenkins, A., Holland, P. R., Ha, H. K., Lee, S. H., Steig, E. J., Ding, Q., Abrahamsen, E. P., and Schröder, M.: Strong Sensitivity of Pine Island Ice-Shelf Melting to Climatic Variability, *Science*, 343, 174-178, doi: 10.1126/science.1244341, 2014.
- Falk, U., and Sala, H.: Winter melt conditions of the inland ice cap on King George Island, Antarctic Peninsula, *Erkunde*, 69, 341-363, doi: 10.3112/erdkunde.2015.04.04, 2015.
- 20 Fernandoy, F., Meyer, H., and Tonelli, M.: Stable water isotopes of precipitation and firn cores from the northern Antarctic Peninsula region as a proxy for climate reconstruction, *The Cryosphere*, 6, 313-330, doi: 10.5194/tc-6-313-2012, 2012.
- Fyfe, J. C., and Saenko, O. A.: Human-Induced Change in the Antarctic Circumpolar Current, *Journal of Climate*, 18, 3068-3073, doi: 10.1175/JCLI3447.1, 2005.
- 25 Fyfe, J. C., Saenko, O. A., Zickfeld, K., Eby, M., and Weaver, A. J.: The Role of Poleward-Intensifying Winds on Southern Ocean Warming, *Journal of Climate*, 20, 5391-5400, doi: 10.1175/2007JCLI1764.1, 2007.
- Gille, S. T.: Decadal-Scale Temperature Trends in the Southern Hemisphere Ocean, *Journal of Climate*, 21, 4749-4765, doi: 10.1175/2008JCLI2131.1, 2008.
- Goodwin, B. P.: Recent Environmental Changes on the Antarctic Peninsula as Recorded in an ice core from the Bruce Plateau, Ph.D. thesis, Graduate Program in Atmospheric Science, Ohio State University, 247 pp., 2013.
- 30 Goodwin, B. P., Mosley-Thompson, E., Wilson, A. B., Porter, S. E., and Sierra-Hernandez, M. R.: Accumulation Variability in the Antarctic Peninsula: The Role of Large-Scale Atmospheric Oscillations and Their Interactions, *Journal of Climate*, 29, 2579-2596, doi: 10.1175/JCLI-D-15-0354.1, 2015.
- Harig, C., and Simons, F. J.: Accelerated West Antarctic ice mass loss continues to outpace East Antarctic gains, *Earth and Planetary Science Letters*, 415, 134-141, doi: 10.1016/j.epsl.2015.01.029, 2015.
- 35 Jiahong, W., Jiancheng, K., Jiankang, H., Zichu, X., Leibao, L., and Dali, W.: Glaciological studies on the King George Island ice cap, South Shetland Islands, Antarctica, *Annals of Glaciology*, 27, 105-109, doi: 10.3198/1998AoG27-1-105-109, 1998.
- Jiankang, H., Jiancheng, K., Jiahong, W., Lluberas, A., and Rodriguez, F.: General characteristics in stratigraphy and density variation for ice cores from Collins Ice Cap, King George Island, Antarctica, *Antarctic Research*, 6, 40-46, 1994.
- Jouzel, J., Delaygue, G., Landais, A., Masson-Delmotte, V., Risi, C., and Vimeux, F.: Water isotopes as tools to document oceanic sources of precipitation, *Water Resources Research*, 49, 7469-7486, doi: 10.1002/2013WR013508, 2013.
- 40 Kanamitsu, M.: Description of the NMC Global Data Assimilation and Forecast System, *Weath. Forecast.*, 4, 335-342, doi: 10.1175/1520-0434(1989)004<0335:DOTNGD>2.0.CO;2, 1989.
- Kennedy, J. J., Rayner, N. A., Smith, R. O., Parker, D. E., and Saunby, M.: Reassessing biases and other uncertainties in sea surface temperature observations measured in situ since 1850: 1. Measurement and sampling uncertainties, *Journal of Geophysical Research: Atmospheres*, 116, n/a-n/a, 10.1029/2010JD015218, 2011a.
- 45 Kennedy, J. J., Rayner, N. A., Smith, R. O., Parker, D. E., and Saunby, M.: Reassessing biases and other uncertainties in sea surface temperature observations measured in situ since 1850: 2. Biases and homogenization, *Journal of Geophysical Research: Atmospheres*, 116, n/a-n/a, 10.1029/2010JD015220, 2011b.
- Kuipers Munneke, P., Picard, G., van den Broeke, M. R., Lenaerts, J. T. M., and van Meijgaard, E.: Insignificant change in 50 Antarctic snowmelt volume since 1979, *Geophysical Research Letters*, 39, doi: 10.1029/2011GL050207, 2012.

- Legrand, M., and Mayewski, P.: Glaciochemistry of polar ice cores: A review, *Rev. Geophys.*, 35, 219-243, doi: 10.1029/96RG03527, 1997.
- Linow, S., Hörhold, M. W., and Freitag, J.: Grain-size evolution of polar firn: a new empirical grain growth parameterization based on X-ray microcomputer tomography measurements, *Journal of Glaciology*, 58, 1245-1252, doi: 10.3189/2012JoG11J256, 2012.
- 5 Marshall, G. J.: Trends in the Southern Annular Mode from observations and Reanalyses, *J. Climate*, 16, 4134-4143, doi: 10.1175/1520-0442(2003)016<4134:TITSAM>2.0.CO;2, 2003.
- Marshall, G. J., Orr, A., van Lipzig, N. P. M., and King, J. C.: The Impact of a Changing Southern Hemisphere Annular Mode on Antarctic Peninsula Summer Temperatures, *J. Climate*, 19, 5388-5404, doi: 10.1175%2FJCLI3844.1, 2006.
- 10 Marshall, G. J.: Half-century seasonal relationships between the Southern Annular Mode and Antarctic temperatures, *Int. J. Climatol.*, 27, 373-383, doi: 10.1002/Joc.1407, 2007.
- Martin, P. J., and Peel, D. A.: The Spatial Distribution of 10 m Temperatures in the Antarctic Peninsula, *Journal of Glaciology*, 20, 311-317, doi: 10.3198/1978JoG20-83-311-317, 1978.
- Masson-Delmotte, V., Hou, S., Ekaykin, A., Jouzel, J., Aristarain, A., Bernardo, R. T., Bromwich, D., Cattani, O., Delmotte, M., Falourd, S., Frezzotti, M., Gallée, H., Genoni, L., Isaksson, E., Landais, A., Helsen, M. M., Hoffmann, G., Lopez, J., Morgan, V., Motoyama, H., Noone, D., Oerter, H., Petit, J. R., Royer, A., Uemura, R., Schmidt, G. A., Schlosser, E., Simoes, J. C., Steig, E. J., Stenni, B., Stievenard, M., van den Broeke, M. R., van de Wal, R. S. W., van de Berg, W. J., Vimeux, F., and White, J. W. C.: A Review of Antarctic Surface Snow Isotopic Composition: Observations, Atmospheric Circulation, and Isotopic Modeling, *J. Climate*, 21, 3359-3387, doi: 10.1175%2F2007JCLI2139.1, 2008.
- 20 Meredith, M., and King, J. C.: Rapid climate change in the ocean west of the Antarctic Peninsula during the second half of the 20th century, *Geophys. Res. Lett.*, 32, 1 - 5, doi: 10.1029/2005GL024042, 2005.
- Meredith, M. P., Stammerjohn, S. E., Venables, H. J., Ducklow, H. W., Martinson, D. G., Iannuzzi, R. A., Leng, M. J., van Wesseem, J. M., Reijmer, C. H., and Barrand, N. E.: Changing distributions of sea ice melt and meteoric water west of the Antarctic Peninsula, *Deep Sea Research Part II: Topical Studies in Oceanography*, doi: 10.1016/j.dsr2.2016.04.019, 2016.
- 25 Meyer, H., Schönicke, L., Wand, U., Hubberten, H. W., and Friedrichsen, H.: Isotope Studies of Hydrogen and Oxygen in Ground Ice - Experiences with the Equilibration Technique, *Isot. Environ. Health. S.*, 36, 133 - 149, doi: 10.1080/10256010008032939, 2000.
- Moser, H., and Stichler, W.: Environmental isotopes in ice and snow, in: *Handbook of environmental isotope geochemistry*, edited by: Fritz, P., and Fontes, J. C., Elsevier, New York, 141-178, 1980.
- 30 Orr, A., Marshall, G. J., Hunt, J. C. R., Sommeria, J., Wang, C.-G., van Lipzig, N. P. M., Cresswell, D., and King, J. C.: Characteristics of Summer Airflow over the Antarctic Peninsula in Response to Recent Strengthening of Westerly Circumpolar Winds, *Journal of the Atmospheric Sciences*, 65, 1396-1413, doi: 10.1175/2007JAS2498.1, 2008.
- Peel, D. A., Mulvaney, R., and Davison, B. M.: Stable-Isotope/Air-Temperature relationship in ice cores from Dolleman Island and the Palmer Land Plateau, Antarctic Peninsula, *Ann. Glaciol.*, 10, 130-136, doi: 10.3198/1988AoG10-130-136, 1988.
- 35 Petit, J. R., White, J. W. C., Young, N. W., Jouzel, J., and Korotkevich, Y. S.: Deuterium Excess in Recent Antarctic Snow, *J. Geophys. Res.-Atmos.*, 96, 5113-5122, doi: 10.1029/90JD02232, 1991.
- Potocki, M., Mayewski, P. A., Kurbatov, A. V., Simões, J. C., Dixon, D. A., Goodwin, I., Carleton, A. M., Handley, M. J., Jaña, R., and Korotkikh, E. V.: Recent increase in Antarctic Peninsula ice core uranium concentrations, *Atmospheric Environment*, 140, 381-385, <http://dx.doi.org/10.1016/j.atmosenv.2016.06.010>, 2016.
- 40 Pritchard, H. D., and Vaughan, D. G.: Widespread acceleration of tidewater glaciers on the Antarctic Peninsula, *J. Geophys. Res.*, 112, F03S29, doi: 10.1029/2006jf000597, 2007.
- Pritchard, H. D., Ligtenberg, S. R. M., Fricker, H. A., Vaughan, D. G., van den Broeke, M. R., and Padman, L.: Antarctic ice-sheet loss driven by basal melting of ice shelves, *Nature*, 484, 502-505, doi: 10.1038/nature10968, 2012.
- 45 Rignot, E., Casassa, G., Gogineni, S., Kanagaratnam, P., Krabill, W., Pritchard, H., Rivera, A., Thomas, R., Turner, J., and Vaughan, D.: Recent ice loss from the Fleming and other glaciers, Wordie Bay, West Antarctic Peninsula, *Geophys. Res. Lett.*, 32, L07502, doi: 10.1029/2004GL021947, 2005.
- Rozanski, K., Araguás-Araguás, L., and Gonfiantini, R.: Isotopic Patterns in Modern Global Precipitation, in: *Climate Change in Continental Isotopic Records*, edited by: Swart, P. K., Lohman, K. C., McKenzie, J., and Savin, S., American Geophysical Union, Washington, USA, 1993.

- Rückamp, M., Blindow, N., Suckro, S., Braun, M., and Humbert, A.: Dynamics of the ice cap on King George Island, Antarctica: field measurements and numerical simulations, *Ann. Glaciol.*, 51, 80-90, 2010.
- Saigne, C., and Legrand, M.: Measurements of methanesulphonic acid in Antarctic ice, *Nature*, 330, 240-242, doi: 10.1038/330240a0, 1987.
- 5 Seehaus, T., Marinsek, S., Helm, V., Skvarca, P., and Braun, M.: Changes in ice dynamics, elevation and mass discharge of Dinsmoor–Bombardier–Edgeworth glacier system, Antarctic Peninsula, *Earth and Planetary Science Letters*, 427, 125-135, doi: 10.1016/j.epsl.2015.06.047, 2015.
- Shepherd, A., Ivins, E. R., A, G., Barletta, V. R., Bentley, M. J., Bettadpur, S., Briggs, K. H., Bromwich, D. H., Forsberg, R., Galin, N., Horwath, M., Jacobs, S., Joughin, I., King, M. A., Lenaerts, J. T. M., Li, J., Ligtenberg, S. R. M., Luckman, A., Luthcke, S. B., McMillan, M., Meister, R., Milne, G., Mouginot, J., Muir, A., Nicolas, J. P., Paden, J., Payne, A. J., Pritchard, H., Rignot, E., Rott, H., Sørensen, L. S., Scambos, T. A., Scheuchl, B., Schrama, E. J. O., Smith, B., Sundal, A. V., van Angelen, J. H., van de Berg, W. J., van den Broeke, M. R., Vaughan, D. G., Velicogna, I., Wahr, J., Whitehouse, P. L., Wingham, D. J., Yi, D., Young, D., and Zwally, H. J.: A Reconciled Estimate of Ice-Sheet Mass Balance, *Science*, 338, 1183-1189, doi: 10.1126/science.1228102, 2012.
- 10
- 15 Sigmond, M., Reader, M. C., Fyfe, J. C., and Gillett, N. P.: Drivers of past and future Southern Ocean change: Stratospheric ozone versus greenhouse gas impacts, *Geophysical Research Letters*, 38, doi: 10.1029/2011GL047120, 2011.
- Simões, J., Ferron, F., Bernardo, R., Aristarain, A., Stievenard, M., Pourchet, M., and Delmas, R.: Ice core study from the King George Island, South Shetlands, Antarctica., *Pesquisa Antártica Brasileira*, 4, 9-23, 2004.
- Sinclair, K. E., Bertler, N. A. N., Trompeter, W. J., and Baisden, W. T.: Seasonality of Airmass Pathways to Coastal Antarctica: Ramifications for Interpreting High-Resolution Ice Core Records, *Journal of Climate*, 26, 2065-2076, doi: 10.1175/JCLI-D-12-00167.1, 2012.
- 20
- Stichler, W., Schotterer, U., Fröhlich, K., Ginot, P., Kull, C., Gäggeler, H., and Pouyaud, B.: Influence of sublimation on stable isotope records recovered from high-altitude glaciers in the tropical Andes, *J. Geophys. Res.*, 106, doi: 10.1029/2001jd900179, 2001.
- 25
- Thomas, E. R., Marshall, G. J., and McConnell, J. R.: A doubling in snow accumulation in the western Antarctic Peninsula, *Geophys. Res. Lett.*, 35, 1-5, doi: 10.1029/2007GL032529, 2008.
- Thomas, E. R., and Bracegirdle, T. J.: Improving ice core interpretation using in situ and reanalysis data, *J. Geophys. Res.*, 114, D20116, doi: 10.1029/2009jd012263, 2009.
- Thomas, E. R., Dennis, P. F., Bracegirdle, T. J., and Franzke, C.: Ice core evidence for significant 100-year regional warming on the Antarctic Peninsula, *Geophys. Res. Lett.*, 36, -, doi: 10.1029/2009gl040104, 2009.
- 30
- Thomas, E. R., and Bracegirdle, T. J.: Precipitation pathways for five new ice core sites in Ellsworth Land, West Antarctica, *Climate Dynamics*, 44, 2067-2078, doi: 10.1007/s00382-014-2213-6, 2015.
- Thompson, D. W. J., and Solomon, S.: Interpretation of Recent Southern Hemisphere Climate Change, *Science*, 296, 895-899, 10.1126/science.1069270, 2002.
- 35
- Travassos, J., and Simoes, J.: High-resolution radar mapping of internal layers of a subpolar ice cap, King George Island, Antarctica, *Pesquisa Antártica Brasileira*, 4, 57-65, 2004.
- Trusel, L. D., Frey, K. E., and Das, S. B.: Antarctic surface melting dynamics: Enhanced perspectives from radar scatterometer data, *Journal of Geophysical Research: Earth Surface*, 117, doi: 10.1029/2011JF002126, 2012.
- Trusel, L. D., Frey, K. E., Das, S. B., Karnauskas, K. B., Kuipers Munneke, P., van Meijgaard, E., and van den Broeke, M. R.: Divergent trajectories of Antarctic surface melt under two twenty-first-century climate scenarios, *Nature Geosci*, 8, 927-932, 10.1038/ngeo2563
- 40
- <http://www.nature.com/ngeo/journal/v8/n12/abs/ngeo2563.html#supplementary-information>, 2015.
- Turner, J., Colwell, S. R., Marshall, G. J., Lachlan-Cope, T. A., Carleton, A. M., Jones, P. D., Lagun, V., Reid, P. A., and Iagovkina, S.: The SCAR READER project: Toward a high-quality database of mean Antarctic meteorological observations, *J. Climate*, 17, 2890-2898, doi: 10.1175/1520-0442(2004)017<2890:TSRPTA>2.0.CO;2, 2004.
- 45
- Turner, J., Colwell, S. R., Marshall, G. J., Lachlan-Cope, T. A., Carleton, A. M., Jones, P. D., Lagun, V., Reid, P. A., and Iagovkina, S.: Antarctic climate change during the last 50 years, *Int. J. Climatol.*, 25, 279-294, doi: 10.1002/joc.1130, 2005.
- Turner, J., Bindschadler, R. A., Convey, P., Di Prisco, G., Fahrbach, E., Gutt, J., Hodgson, D. A., Mayewski, P. A., and Summerhayes, C. P.: Antarctic Climate Change and the Environment, Scott Polar Research Institute, Scientific Committee on Antarctic Research, Cambridge, UK, 2009.
- 50

- Turner, J., Lu, H., White, I., King, J. C., Phillips, T., Hosking, J. S., Bracegirdle, T. J., Marshall, G. J., Mulvaney, R., and Deb, P.: Absence of 21st century warming on Antarctic Peninsula consistent with natural variability, *Nature*, 535, 411-415, doi: 10.1038/nature18645, 2016.
- 5 Uemura, R., Matsui, Y., Yoshimura, K., Motoyama, H., and Yoshida, N.: Evidence of deuterium excess in water vapor as an indicator of ocean surface conditions, *J. Geophys. Res.*, 113, 1-10, doi: 10.1029/2008JD010209, 2008.
- van Lipzig, N. P. M., Marshall, G. J., Orr, A., and King, J. C.: The Relationship between the Southern Hemisphere Annular Mode and Antarctic Peninsula Summer Temperatures: Analysis of a High-Resolution Model Climatology, *Journal of Climate*, 21, 1649-1668, 10.1175/2007JCLI1695.1, 2008.
- 10 van Wessem, J. M., Reijmer, C. H., van de Berg, W. J., van den Broeke, M. R., Cook, A. J., van Ulf, L. H., and van Meijgaard, E.: Temperature and Wind Climate of the Antarctic Peninsula as Simulated by a High-Resolution Regional Atmospheric Climate Model, *Journal of Climate*, 28, 7306-7326, doi: 10.1175/JCLI-D-15-0060.1, 2015.
- Yaorong, H., Zhenhe, X., and Cong, X.: A Study on Snowstorm Weather in Coastal Area of Western Antarctic, *Marine Science Bulletin*, 5, 24-31, 2003.
- 15 Zagorodnov, V., Nagornov, O., Scambos, T. A., Muto, A., Mosley-Thompson, E., Pettit, E. C., and Tyufin, S.: Borehole temperatures reveal details of 20th century warming at Bruce Plateau, Antarctic Peninsula, *The Cryosphere*, 6, 675-686, 10.5194/tc-6-675-2012, 2012.
- Zamoruyev, V. V.: Results of glaciological observations at Bellingshausen station in 1968, *Trudy Sovetskoy Antarkticheskoy Ekspeditsii*, 55, 135-144, 1972.

20

25

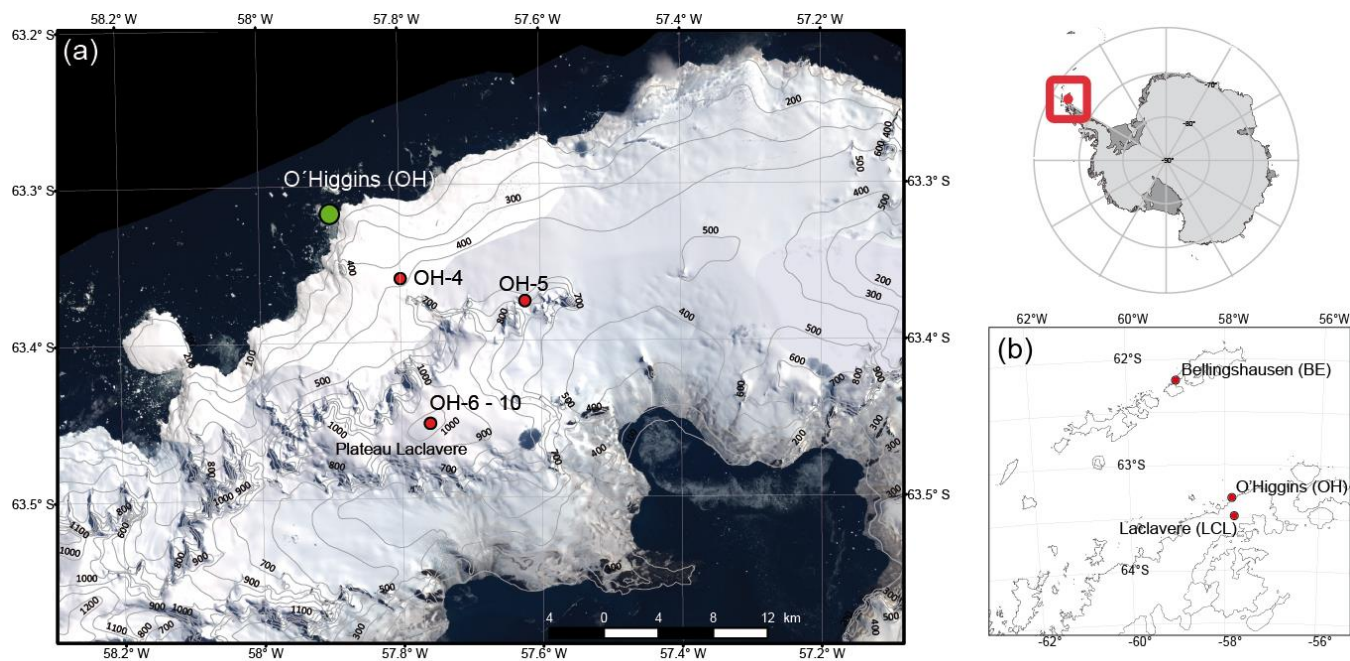


**Figure 1:** Investigation area and location of the firm cores presented in this work. (a) Detail of the study zone: the green point shows the Chilean Station O'Higgins (OH) at the west coast of the Antarctic Peninsula. Firn cores retrieved between 2008 and 2015 are shown by red dots. (b) Location of O'Higgins and Bellingshausen Station and Laclavere Plateau, which are mentioned through the text. Satellite image (Landsat ETM+) and digital elevation model (RADARSAT) available from the Landsat Image Mosaic of Antarctica (LIMA) (<http://lima.usgs.gov/>).

5

10

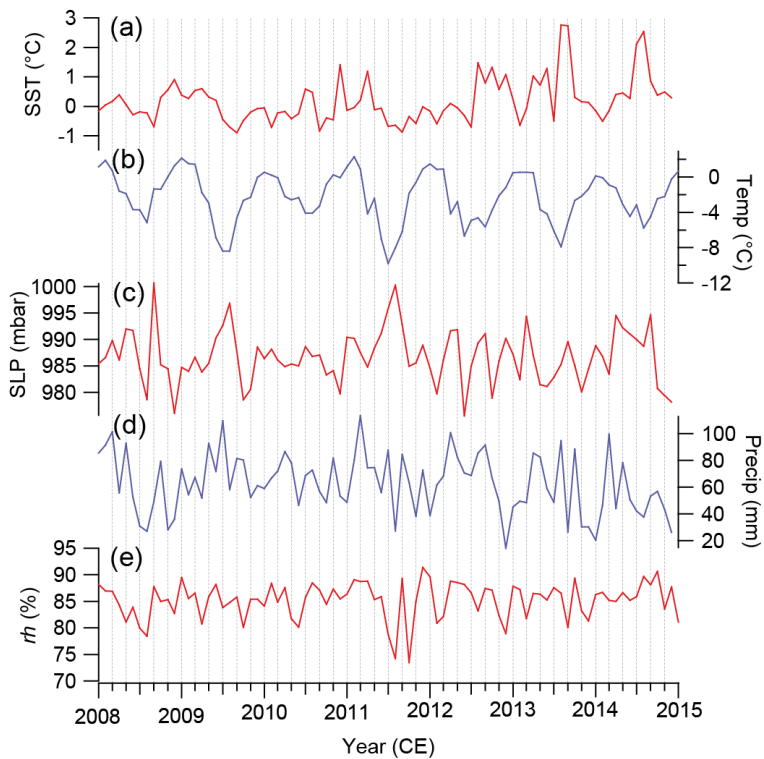


**Figure 2:** Meteorological data sets used in this study, (a) Sea surface temperature (SST), (b) Air temperature (Temp), (c) Sea level pressure (SLP) and (d) Precipitation amount (Precip) from Bellingshausen Station (BE) on King George Island and (e) Relative humidity (*rh*) from the Southern Ocean surrounding the northern Antarctic Peninsula (AP) region. Data shown in the figure is available from the READER dataset (<https://legacy.bas.ac.uk/met/READER/>) (Turner et al., 2004).

5

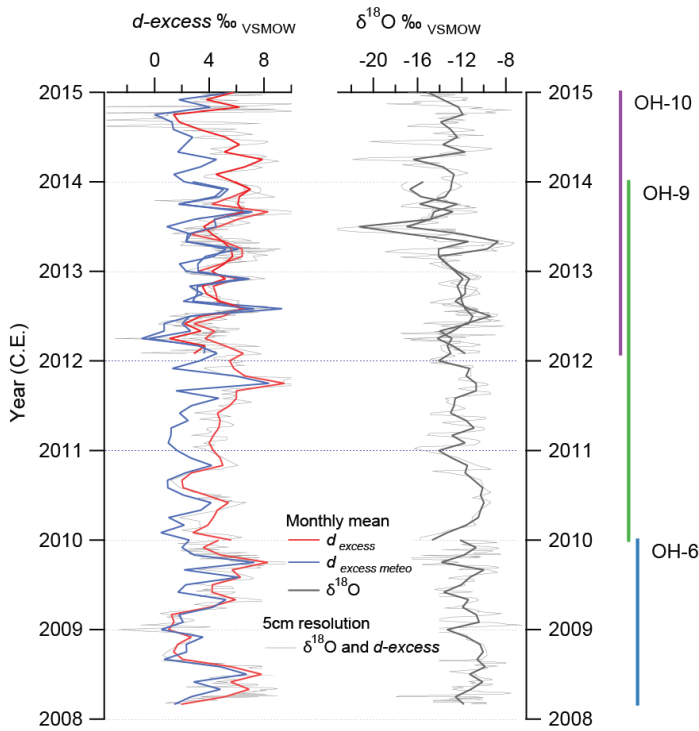


**Figure 3:** Time series for firn cores OH-6 (light blue line right), OH-9 (green light right) and OH-10 (purple line right) derived for  $\delta^{18}\text{O}$  (black line right) and  $d_{\text{excess}}$  (red line left) records using a theoretical  $d_{\text{excess}}$  ( $d_{\text{excess meteo}}$ ) value (blue line left). The  $d_{\text{excess meteo}}$  is calculated from Sea surface temperature (SST) and Relative Humidity ( $rh$ ) according to Uemura et al. (2008). All three cores are located at the same location within the GPS navigator horizontal error (<10m).

5



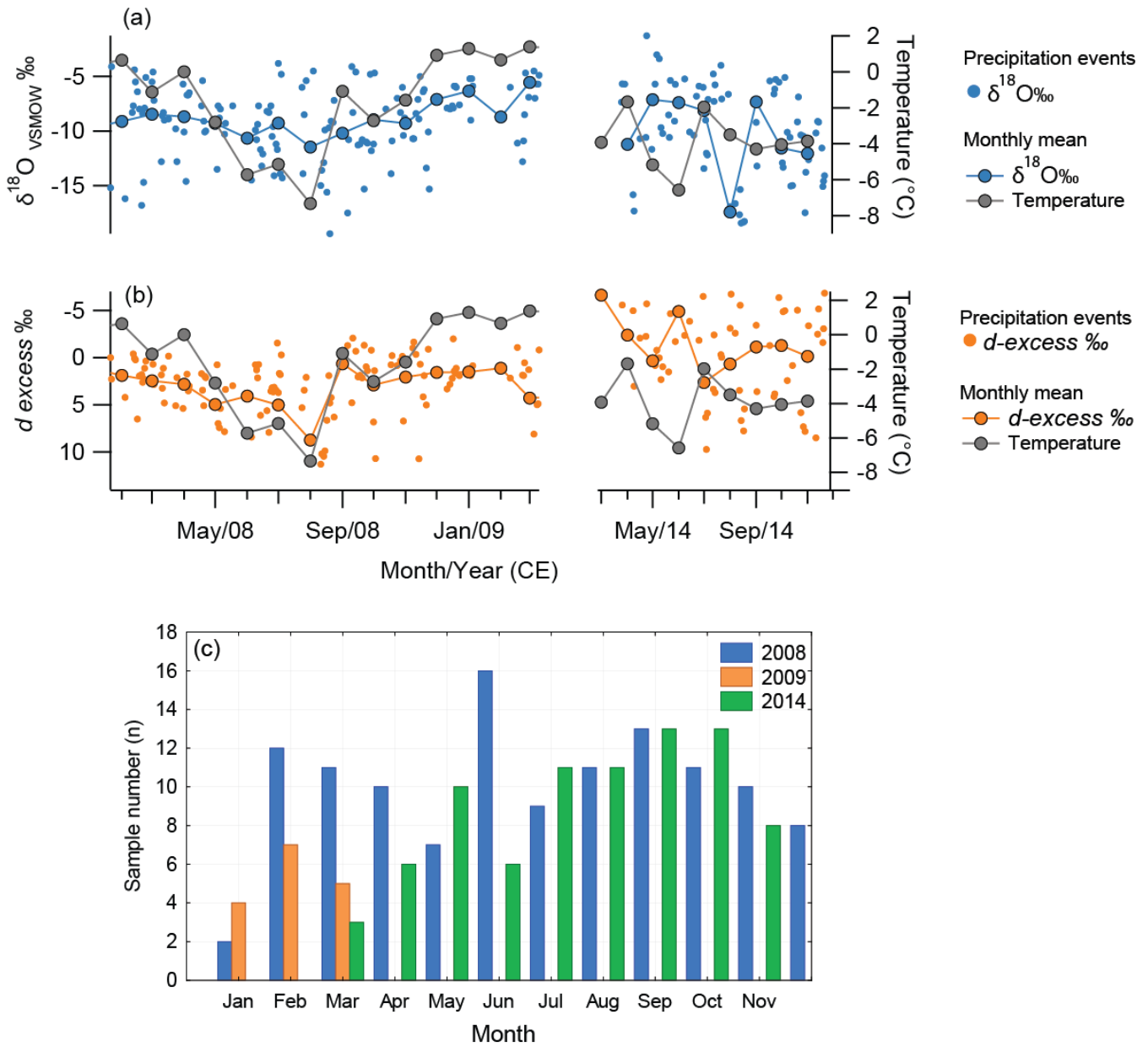


**Figure 4:** Stable water isotope composition of precipitation events and air temperature at O'Higgins Station. (a) shows the  $\delta^{18}\text{O}$  composition of precipitation of single daily events (small solid blue dots) and monthly means (big solid blue dots and line) and (b) deuterium excess ( $d_{\text{excess}}$ ) of single daily events (small orange dots) and monthly means (big orange dots and line). In both (a) and (b) monthly mean air temperature is also shown (grey solid dots and line). (c) Histogram showing the monthly distribution of precipitation samples (n) collected at O'Higgins Station in 2008, 2009 and 2014

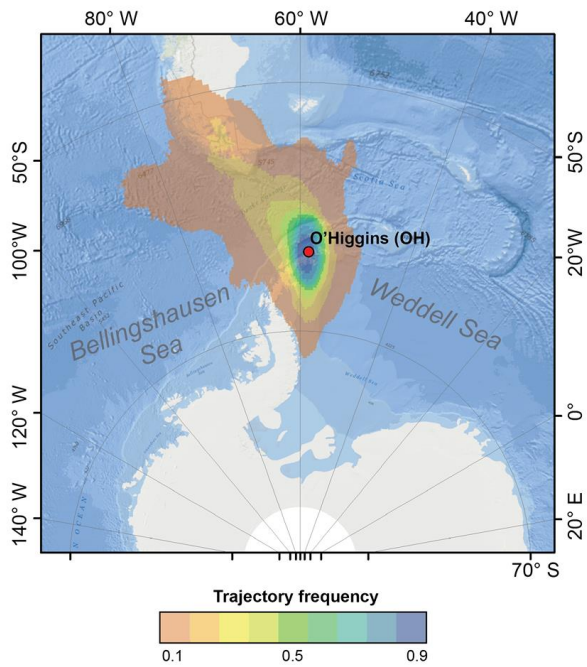


**Figure 5:** Frequency distribution map of the main transport paths of air masses approaching the northern Antarctic Peninsula (AP). Translucent red colours represent the lowest frequency and blue colours the higher frequency. In general most of the air masses arriving at the AP are coming from the Bellingshausen Sea and the South Pacific Ocean.

5

10

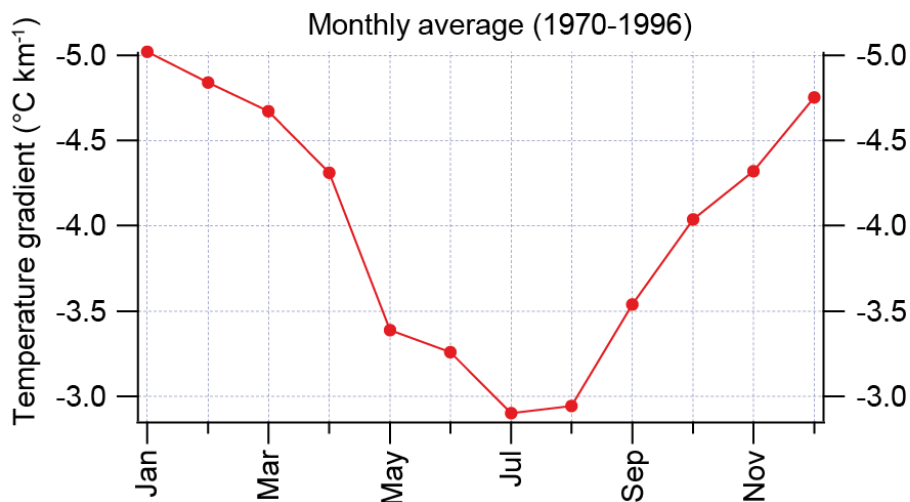


**Figure 6:** Temperature lapse rate from sea level to 850 hPa level at Bellingshausen station (BE), King George Island, Antarctica. The data is shown as the monthly mean value of observation between 1979 and 1996 (SCAR Reference Antarctic Data for Environmental Research).

5

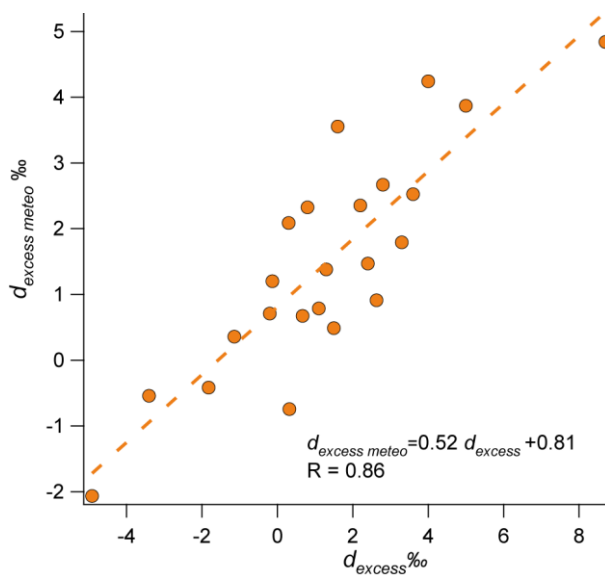


**Figure 7:** Correlation between monthly mean deuterium excess values ( $d_{excess}$ ) from precipitation samples and theoretical deuterium excess values calculated from meteorological parameters of the moisture source region ( $d_{excess\ meteo}$ ) according to Uemura et al. (2008).

10

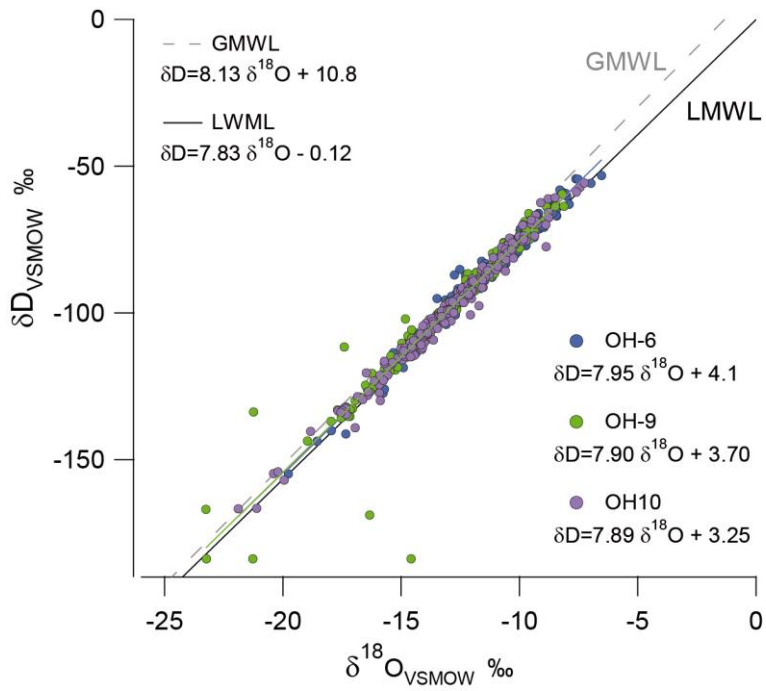
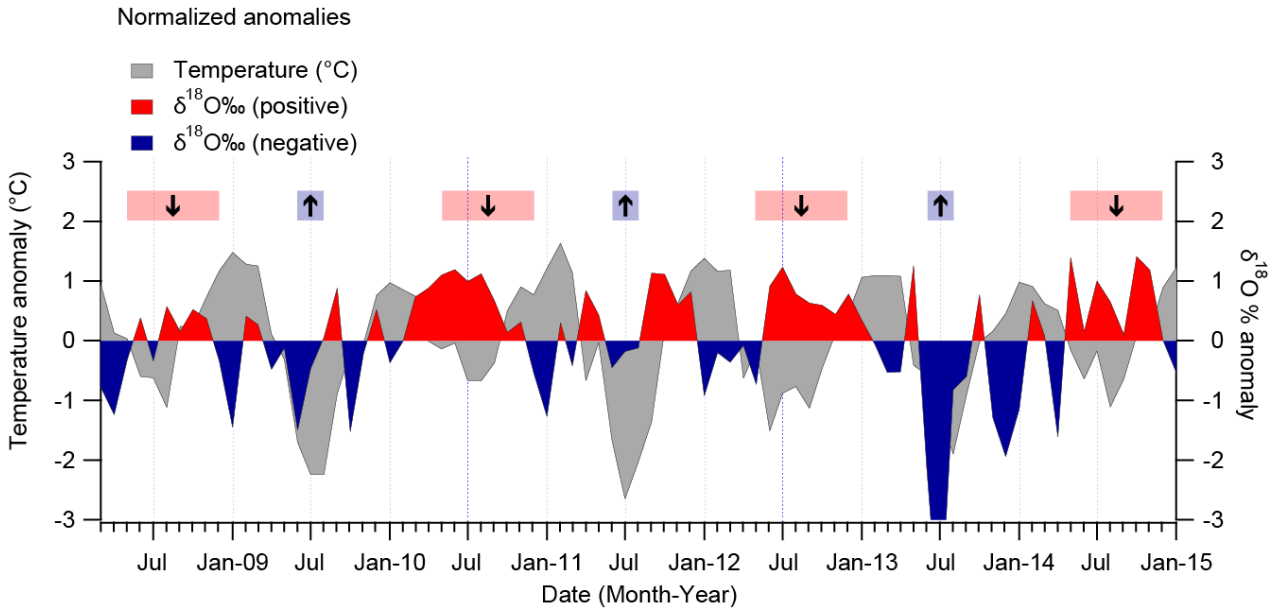
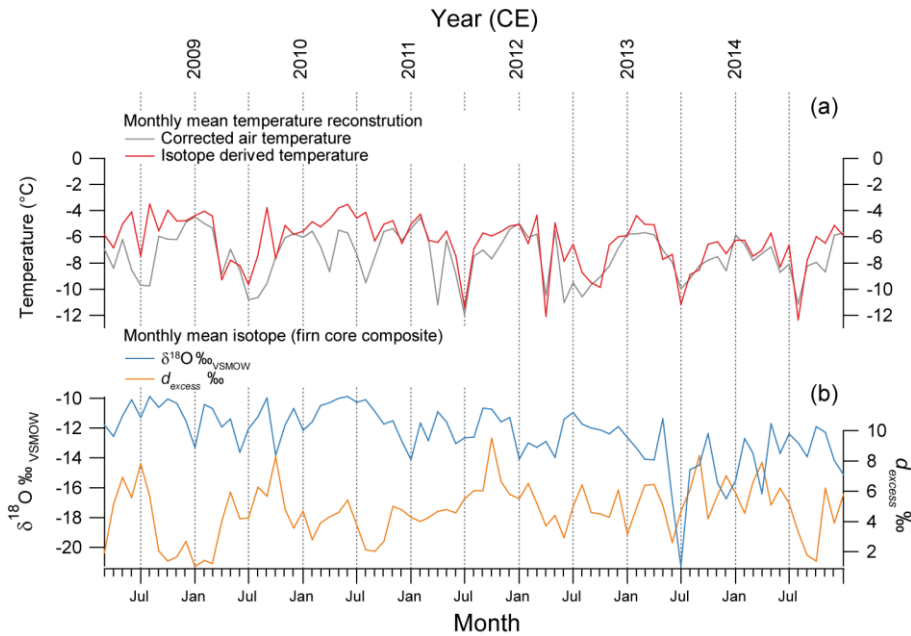


**Figure 8:** Co-isotopic relationship of firn cores OH-6 (solid blue dots), OH-9 (solid green dots) and OH-10 (solid purple dots). All slopes and intercepts are very close to each other as well as to the global and local meteoric water line (GMWL – grey dashed line, and LMWL – black solid line, respectively). Stable water isotope analysis for each firn core was made at 5cm resolution, representing 630 samples in total.

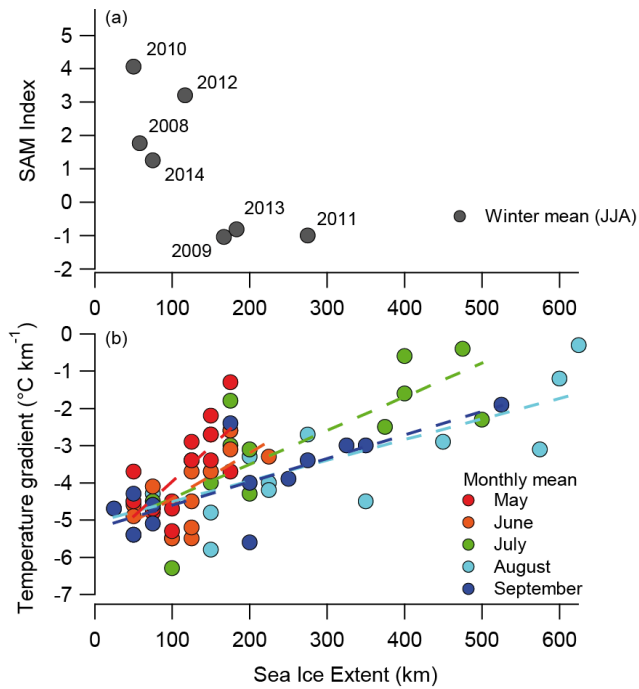


5 **Figure 9:** Standardized anomalies for air (monthly mean) temperatures (solid grey colours) registered at Bellingshausen Station (BE) on King George Island and a composite  $\delta^{18}\text{O}$  time series derived from firn cores OH-6, OH-9 and OH-10 from Laclavere Plateau (LCL). Upper translucent red (blue) boxes show period of positive (negative) anomalies, down (up) arrow shows the inverse (positive) stable water isotope – temperature relationship Both time series were detrended prior to constructing the time series of anomalies.



10 **Figure 10:** (a) Monthly mean air temperature reconstruction for LCL between March 2008 and January 2015 based on air temperature corrected by a seasonal factor and altitudinal gradient (grey line) and based on a  $\delta^{18}\text{O}$  composite time series derived from firn cores from

LCL corrected by a seasonal factor (red line), respectively. (b)  $\delta^{18}\text{O}$  and  $d_{\text{excess}}$  monthly mean composite time series of LCL firn cores used for the temperature reconstruction of the upper panel.



5 **Figure 11:** Sea ice extent (SIE) from O'Higgins Station (OH) and its relationship to (a) the Southern Annular Mode and (b) to the temperature gradient between sea level and 1100 m a.s.l. at the Laclavere Plateau (LCL). SIE data is from the National Snow & Ice Data Center data set (NSIDC). Sea ice extent, defined as the extension of the sea region covered for at least 15% of ice, exhibits a negative relationship to the Southern Annular Mode between 2008 and 2014. The relationship to the temperature gradient is positive. A decreasing seasonal pattern of the temperature gradient can be observed from May to September (1979 – 1996).

10

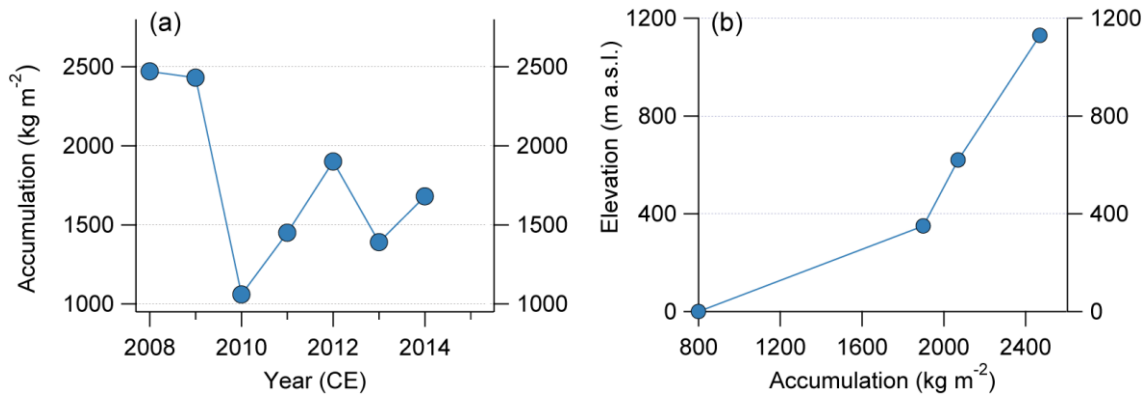
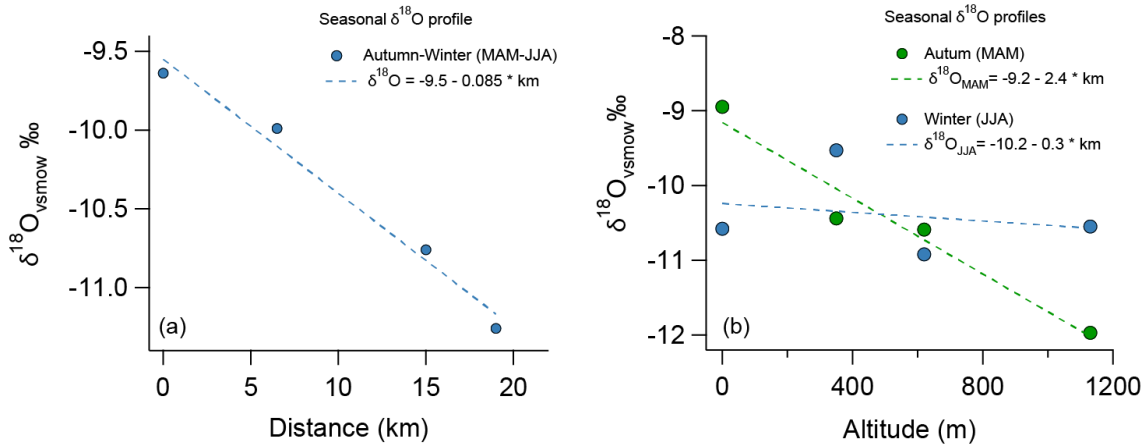
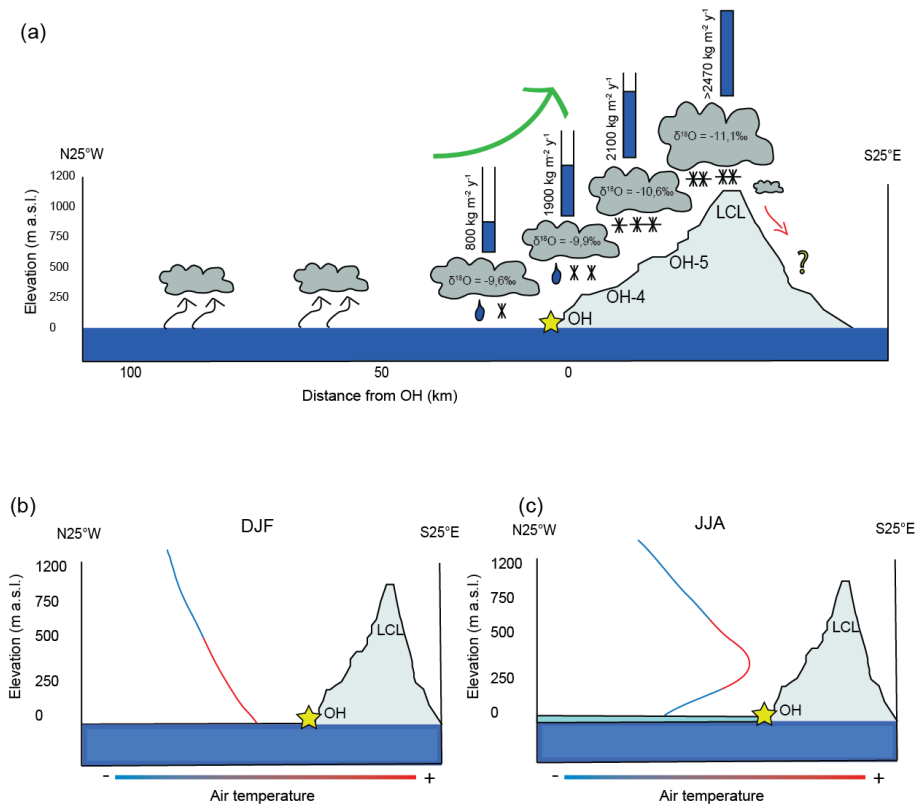


**Figure 12:** (a) Accumulation rates for Plateau Laclavere during 2008 – 2014 estimated from the stable water isotope composition of firn cores OH-6, OH-9 and OH-10 and their respective density profiles. (b) Accumulation variability for the west flank of the northern Antarctic

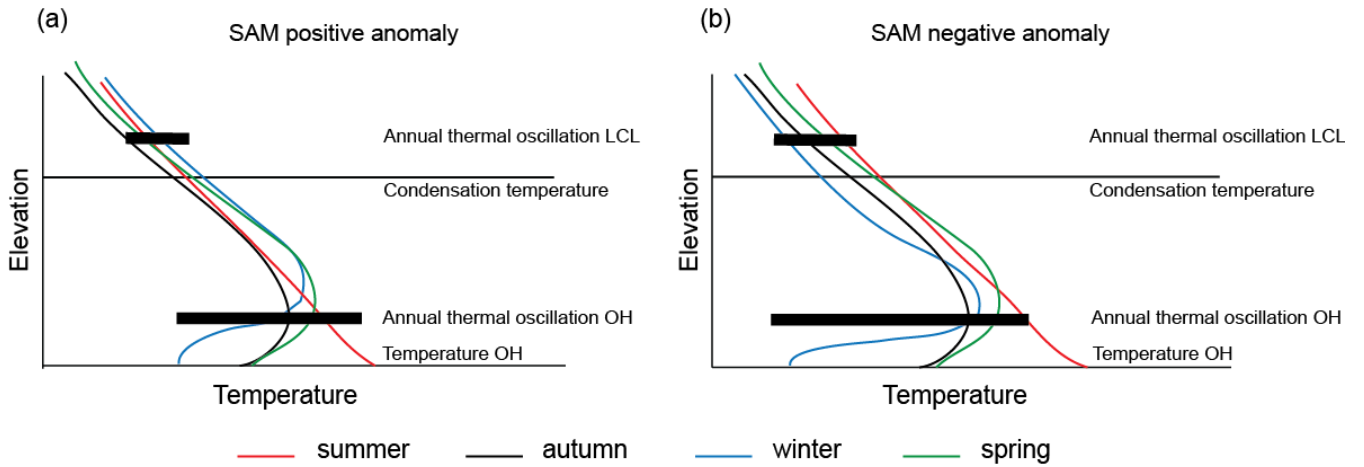
Peninsula from the coast to Laclavere Plateau. Accumulation rates were derived from precipitation at O'Higgins Station at sea level and firn cores (OH-4, OH-5 and OH-6) for higher altitudes.



5 **Figure 13:**  $\delta^{18}\text{O}$  profile with relation to (a) the distance from the coast at O'Higgins Station (OH) and at different points on the west flank of the AP (6.5 km (OH-4), 15 km (OH-5) and 19 km (OH-6)) and (b) altitude at 350 m (OH-4), 620 m (OH-5) and 1130 m a.s.l. (OH-6) during autumn (MAM) (green solid dots) and winter (JJA) (blue solid dots).



5 **Figure 14:** (a) Schematic chart showing the orographic barrier effect of the AP on the stable water isotope depletion and accumulation rate at different altitudes, firn core locations (OH-4, OH-5 and OH-6) and distances from the coast (OH); (b) temperature gradient (adiabatic cooling) during DJF (summer) and sea-ice-free conditions; (c) inversion layer in the lower troposphere during sea-ice-covered conditions in JJA (winter).



10 **Figure 15:** Sea level to LCL temperature oscillation scheme during summer (DJF), autumn (MAM), winter (JJA) and spring under: (a) positive SAM anomaly conditions and (b) negative SAM anomaly conditions.

15

20

25



**Table 1:** Statistical summary of the geographical location and water stable isotope composition of all firn cores examined in this work. OH-4 and OH-5 correspond to cores retrieved on the west side of the AP, whereas OH-6, OH-9 and OH-10 were retrieved at LCL on the east-west divide. All cores were analyzed in a 5 cm resolution.

Core	OH-4	OH-5	OH-6	OH-9	OH-10
Coordinates	57.80°W, 63.36°S	57.62°W, 63.38°S	57.76°W, 63.45°S	57.76°W, 63.45°S	57.76°W, 63.45°S
Altitude (m a.s.l.)	350	620	1130	1130	1130
Depth (m)	15.75	10.6	11.02	11.65	10.17
Drilling date	Jan 2009	Jan 2009	Jan 2010	Jan 2014	Jan 2015
$\delta^{18}\text{O}$ (‰)					
Mean	-10.4	-10.2	-12.0	-12.80	-12.94
Sdev	1.2	1.5	2.5	2.53	2.57
Min	-14.1	-14.2	-19.8	-23.25	-21.88
Max	-7.0	-7.2	-6.5	-8.12	-7.25
$\delta\text{D}$ (‰)					
Mean	-78.9	-78.1	-91.4	-97.49	-98.81
Sdev	9.7	12.0	19.4	21.04	20.45
Min	-108.2	-111.2	-154.9	-183.80	-166.82
Max	-54.0	-52.1	-53.2	-59.62	-55.80
$d_{\text{excess}}$ (‰)					
Mean	4.0	3.9	4.4	5.11	4.72
Sdev	1.5	1.7	2.8	1.90	2.66
Min	0.5	-0.6	-2.6	0.00	-6.50
Max	8.6	8.2	15.0	10.97	11.27
n (samples)	318	213	208	232	190

10

15

**Table 2:** Statistics of the stable water isotope composition of precipitation samples collected at OH Station on the AP 2008–2009 and 2014.

Station	O'Higgins	O'Higgins
Sampling interval	Feb 2008 – Mar 2009	Apr – Nov 2014
Coordinates	63.32°S, 57.90°W	63.32°S, 57.90°W
$\delta^{18}\text{O}$ (‰)		
Mean	-9.2	-10.12
Sdev	3.33	4.39
Min	-19.4	-18.43
Max	-3.8	-1.28
$\delta\text{D}$ (‰)		
Mean	-70.5	-81.86
Sdev	26.44	34.21
Min	-150.6	-148.36
Max	-21.8	-15.99
$d_{\text{excess}}$ (‰)		
Mean	2.7	3.84
Sdev	4.15	4.67
Min	-6.6	-1.75
Max	22.3	14.70
n (samples)	139	69

5

**Table 3:** Correlation between deuterium excess ( $d_{\text{excess meteo}}$ ) values calculated from monthly mean meteorological data (SST and  $rh$ ) and water stable isotope monthly means for all cores used in this study.

Core	OH-4	OH-5	OH-6	OH-9	OH-10
Time interval	Jan 2006 – Jan 2009	Mar 2007 – Jan 2009	Mar 2008 – Jan 2010	Feb 2010 – Jan 2014	Feb 2012 – Jan 2015
Corr. coefficient	0.72	0.79	0.81	0.78	0.67
p-value	<0.01	<0.01	<0.01	<0.01	<0.01

10

**Table 4:** Accumulation rates calculated for all firn cores used in this study. All rates are shown as seasonal and annual mean values with respect to the time interval covered by each core.

	AP Accumulation (kg m <sup>-2</sup> )				
	Western Flank		LCL		
	OH-4	OH-5	OH-6	OH-9	OH-10
DJF-MAM	1121				
JJA-SON	1300				
<b>2006</b>	<b>2510</b>				
DJF-MAM	1650	>1380			
JJA-SON	1300	1150			
<b>2007</b>	<b>2950</b>	<b>&gt;2530</b>			
DJF-MAM	1130	1020	>1530		
JJA-SON	770	1050	940		
<b>2008</b>	<b>1900</b>	<b>2070</b>	<b>&gt;2470</b>		
DJF-MAM			1090		
JJA-SON			1340		
<b>2009</b>			<b>2430</b>		
DJF-MAM			700		
JJA-SON			360		
<b>2010</b>			<b>1060</b>		
DJF-MAM			680		
JJA-SON			770		
<b>2011</b>			<b>1450</b>		
DJF-MAM			1170	1080	
JJA-SON			730	690	
<b>2012</b>			<b>1900</b>	<b>1770</b>	
DJF-MAM			890	930	
JJA-SON			500	690	
<b>2013</b>			<b>1390</b>	<b>1620</b>	
DJF-MAM				630	
JJA-SON				1050	
<b>2014</b>				<b>1680</b>	

5